

THE SOLUTION STRUCTURES OF TWO HUMAN IgG1 ANTIBODIES SHOW CONFORMATIONAL STABILITY AND ACCOMMODATE THEIR C1q AND FcγR LIGANDS

Lucy E. Rayner^{1*}, Gar Kay Hui^{1*}, Jayesh Gor¹, Richard K. Heenan², Paul A. Dalby³ and Stephen J. Perkins^{1‡}

* These authors contributed equally to this work.

From the ¹Department of Structural and Molecular Biology, Division of Biosciences, Darwin Building, University College London, Gower Street, London WC1E 6BT, U.K.; ²ISIS Facility, Science and Technology Facilities Council, Rutherford Appleton Laboratory, Harwell Oxford, Didcot, OX11 0QX, U. K.; ³Department of Biochemical Engineering, Division of Engineering, Roberts Building, University College London, Gower Street, London WC1E 7JE, U.K.

Running Title: Solution structure of IgG1

***Address correspondence to:** Prof. S. J. Perkins, Department of Structural and Molecular Biology, Darwin Building, University College London, Gower Street, London, WC1E 6BT, U.K. Tel: 020-7679-7048, FAX: 020-7679-7193; Email: s.perkins@ucl.ac.uk.

Keywords: Analytical ultracentrifugation, antibody, constrained modelling, neutron scattering, human IgG1, X-ray scattering.

Background: The human IgG1 antibody subclass is the most abundant one and is widely used in therapeutic applications.

Results: Ultracentrifugation and X-ray/neutron scattering, together with atomistic modelling, revealed asymmetric concentration-independent IgG1 solution structures.

Conclusion: The complement and receptor Fc binding sites are not hindered by the Fab regions, explaining its full activity.

Significance: These solution structures clarify IgG1 activity and its therapeutic applications.

The human IgG1 antibody subclass shows distinct properties compared to the IgG2, IgG3 and IgG4 subclasses, and is the most exploited subclass in therapeutic antibodies. It is the most abundant subclass, has a half-life as long as that of IgG2 and IgG4, binds the FcγR receptor, and activates complement. There is limited structural information on full-length human IgG1 because of the challenges of crystallisation. To rectify this, we have studied the solution structures of two human IgG1 6a and 19a monoclonal antibodies in different buffers at different temperatures. Analytical ultracentrifugation showed that both antibodies were predominantly monomeric, with sedimentation coefficients $s_{20,w}^0$ of 6.3 S

- 6.4 S. Only a minor dimer peak was observed, and the amount was not dependent on buffer conditions. Solution scattering showed that the X-ray radius of gyration R_g increased with salt concentration, while the neutron R_g values remained unchanged with temperature. The X-ray and neutron distance distribution curves $P(r)$ revealed two peaks, $M1$ and $M2$, whose positions were unchanged in different buffers to indicate conformational stability. Constrained atomistic scattering modelling revealed predominantly asymmetric solution structures for both antibodies with extended hinge structures. Both structures were similar to the only known crystal structure of full-length human IgG1. The Fab conformations in both structures were suitably positioned to permit the Fc region to bind readily to its FcγR and C1q ligands without steric clashes, unlike human IgG4. Our molecular models for human IgG1 explain its immune activities, and we discuss its stability and function for therapeutic applications.

IgG1 is the most abundant human IgG antibody subclass (8 mg/ml) of the four found in serum. Following high specificity and affinity binding of the antigen to their Fab regions, the immune

response and effector functions are mediated through the Fc region. IgG1 binds to every class of Fc γ receptor (Fc γ R) found on immune effector cells, and activates the complement cascade when C1q is recruited by several Fc regions (1). Binding to Fc γ Rs on immune cell surfaces leads to diverse immune responses, including antibody-dependent cell-mediated cytotoxicity, to clear foreign antigen from the body. IgG1 has been extensively studied, making it the most understood and exploited human IgG subclass for the development of therapeutic antibodies. Over thirty IgG monoclonal antibodies have been approved as of June 2012 for clinical use by the Food and Drug Administration, of which 68% of marketed and late-stage clinical phase therapeutic antibodies involve the human IgG1 subclass (2).

The four human IgG subclasses IgG1-IgG4 vary primarily in the hinge region, which connects the Fab and Fc regions together, and contributes flexibility at these central regions. The hinge length is linked with IgG functionality. The hinge is best considered as a three-part structure, in which the upper and middle hinge sections of IgG1, IgG2, IgG3 and IgG4 contain 15, 12, 62 and 12 amino acids respectively. The order of flexibility is IgG3 > IgG1 > IgG4 > IgG2 which correlates well with the hinge length (3,4). The upper hinge determines the arrangement between the two Fab regions and mediates flexibility and reorientations of each Fab arm; this allows IgG1 to bind to multiple antigens in different positions (5). Two cysteine residues (Cys²²⁶ and Cys²²⁹) in the middle hinge form interchain disulphide bonds between the two heavy chains to join these together (Fig. 1). The lower hinge is responsible for the flexibility and positioning of the Fc region relative to the Fab arms and affects the binding of Fc to Fc γ R (5,6).

Only limited structural information is available for full-length IgG antibodies. These are difficult to crystallise for reason of the flexible domain arrangements found in IgG. Thus hinge-deleted human IgG1 structures solved by X-ray crystallography include IgG1 Dob and Mcg (7-9). These revealed symmetric IgG structures that are not a true picture of wild-type antibody conformations. The crystal structure of a full-length human IgG1 b12 has been reported alongside full-length murine IgG1 and

IgG2a (10-12). Human IgG1 b12 showed an asymmetric structure with extended hinges, although atomic coordinates for part of one of the hinge regions is missing. These crystal structures necessarily contain IgG held in a fixed position by intermolecular contacts within the crystallographic unit cell, offering only a single snapshot of the multiple conformations expected in solution (13). The advent of atomistic constrained scattering modelling has mitigated this issue. Thus human IgG4, IgA1 and IgA2, IgD and IgM have been studied successfully in physiological buffers, and molecular structures have been determined in Protein Data Bank coordinate formats (14-19).

Solution structures for the human IgG1 subclass are essential to understand its function and stability in the human body, especially for therapeutic applications. Joint X-ray and neutron scattering studies rectify the limitation of the single available IgG1 b12 crystal structure by enabling the study of different buffer and solution conditions on the IgG1 structure. The recent advent of high-throughput X-ray measurements provides hundreds of scattering curves in a single measurement session, and these permit atomistic antibody structures to be determined for a broad range of solution conditions. Here we report solution structures for two IgG1 antibodies, IgG1 6a and IgG1 19a, with known sequences (Fig. 2). Both IgG1 were found to be predominantly monomeric in all buffer conditions tested. Both IgG1 solution structures displayed semi-extended asymmetric arrangements of the Fab regions relative to the Fc region. These structures become more elongated with increase in salt concentration. By reference to the crystal structure of a Fc γ R-Fc complex and a docked structural model for C1q binding to Fc, it could be assessed whether the Fab regions in both IgG1 solution structures allowed enough space for the Fc γ R and C1q ligands to bind to the top of the Fc region in IgG1. The successful outcome of our analyses accounted for the reactivity of IgG1 for Fc γ R and C1q. This is in marked distinction to our recent similar analyses for human IgG4, where this binding to the Fc region was most likely sterically hindered by the Fab regions (15). Previously, conformational instabilities were found in IgG4 (15); it is therefore also crucial to identify whether or not IgG1 is also affected by the same instabilities that occur in IgG4.

EXPERIMENTAL PROCEDURES

Purification and composition of IgG1 - Both IgG1 6a and IgG1 19a were generously supplied by Dr Bryan Smith at UCB (<https://www.ucb.com>). Immediately prior to measurements, both were further purified by gel filtration to remove non-specific aggregates using a Superose 6 10/300 column (GE Healthcare), then concentrated using Amicon Ultra spin concentrators (50 kDa molecular mass cut-off), and dialyzed at 4°C against the appropriate ultracentrifugation and scattering buffer (see below). The sequence identity for the two IgG1 molecules was 100 % for the C_{H1}, C_{H2}, C_{H3} and C_L domains. Differences in sequences were found in the V_H (65.2%) and V_L (73.2%) domains. Total sequence identity between the two IgG1 forms was 88.7% (Fig. 2). The N-linked oligosaccharides at Asn²⁹⁷ on the C_{H2} domains (Fig. 2) were assumed to have a typical complex-type biantennary oligosaccharide structure with a Man₃-GlcNAc₂ core and two NeuNAc.Gal.GlcNAc antennae (20). The IgG1 6a molecular mass was calculated to be 150.1 kDa, its unhydrated volume was 193.1 nm³, its hydrated volume was 254.4 nm³ (based on a hydration of 0.3g of water per gram of glycoprotein and an electrostricted volume of 0.0245 nm³ per bound water molecule), its partial specific volume ν was 0.729 ml/g, and its absorption coefficient at 280 nm was 15.4 (1%, 1 cm path length) (21). Likewise, IgG1 19a has a calculated molecular mass of 149.7 kDa, an unhydrated volume of 192.4 nm³, a hydrated volume of 253.5 nm³, a ν of 0.728 ml/g and an absorption coefficient at 280 nm of 15.6 (1%, 1 cm path length).

All data were recorded in phosphate-buffered saline with different NaCl concentrations. That termed PBS-137 has a composition of 137 mM NaCl, 8.1 mM Na₂HPO₄, 2.7 mM KCl and 1.5 mM KH₂PO₄ (pH 7.4). When 137 mM NaCl was replaced by 50 mM NaCl or 250 mM NaCl, these were termed PBS-50 or PBS-250, respectively. The buffer densities were measured using an Anton Paar DMA 5000 density meter, and compared with the theoretical values calculated by SEDNTERP (22). This resulted in densities of 1.00530 g/ml for PBS-137 at 20°C (theoretical, 1.00534 g/ml), 1.00189 g/ml for PBS-50 at 20°C (theoretical, 1.00175 g/ml), 1.01003 g/ml for PBS-250 at 20°C (theoretical, 1.00998 g/ml)

and 1.11238 g/ml for PBS-137 at 20°C in 100% ²H₂O.

Sedimentation velocity data for IgG1 - Analytical ultracentrifugation data for IgG1 6a were obtained on two Beckman XL-I instruments equipped with AnTi50 rotors. Sedimentation velocity data were acquired for IgG1 samples in PBS-50, PBS-137 and PBS-250 at 20°C (H₂O) and in PBS-137 with 100% ²H₂O. Sedimentation velocity data were acquired for IgG1 19a only in PBS-137 (H₂O) at 20°C. Data were collected at rotor speeds of 40,000 rpm and 50,000 rpm in two-sector cells with column heights of 12 mm. Sedimentation analysis was performed using direct boundary Lamm fits of up to 745 scans using SEDFIT (version 14.1) (23,24). SEDFIT resulted in size-distribution analyses $c(s)$ that assume all species to have the same frictional ratio f/f_0 . The final SEDFIT analyses used a fixed resolution of 200 and optimized the $c(s)$ fit by floating f/f_0 and the baseline until the overall root-mean-square deviations and visual appearance of the fits were satisfactory. The percentage of oligomers in the total loading concentration was derived using the $c(s)$ integration function.

X-ray and neutron scattering data for IgG1 - X-ray scattering data were obtained during a beam session in 16-bunch mode on Instrument ID02 at the European Synchrotron Radiation Facility, Grenoble, France, operating with a ring energy of 6.0 GeV on the Beamline ID02 (25). Data were acquired using a fast readout low noise camera (FreLoN) with a resolution of 512×512 pixels. A sample-to-detector distance of 3.0 m was used. Both IgG1 6a and IgG1 19a were studied in PBS-50, PBS-137 and PBS-250 at 20°C. IgG1 6a was studied at four concentrations between 0.5-2.0 mg/ml for each condition, and also at 4 mg/ml in PBS-137. IgG1 19a was studied at six concentrations between 0.22-1.35 mg/ml in PBS-50, between 0.30-1.89 mg/ml in PBS-137 and between 0.26-1.62 mg/ml in PBS-250. Sample volumes of 100 μ l were measured in a polycarboxylate capillary of diameter 2 mm that avoids protein deposits during exposures, with the sample being moved continuously during beam exposure to reduce radiation damage. Sets of 10 time frames, with a frame exposure time of 0.1 s or 0.2 s each, were acquired in quadruplicate as a control of reproducibility. Online checks during data acquisition confirmed the absence

of radiation damage, after which the 10 frames were averaged.

Neutron scattering data were obtained on Instrument SANS2D at the ISIS pulsed neutron source at the Rutherford Appleton Laboratory, Didcot, UK (26). A pulsed neutron beam was derived from proton beam currents of $\sim 40 \mu\text{A}$. SANS2D data were recorded with 4 m of collimation, a 4 m sample-to-detector distance, a 12 mm beam diameter and a wavelength range of 0.175 - 1.65 nm made available by time-of-flight. Samples were measured in 2 mm path length circular banjo cells for 1-2 h in a thermostated rack at 6°C, 20°C and 37°C. Data were only collected for IgG1 6a at three concentrations between 2.0-4.0 mg/ml in PBS-137 in 100% $^2\text{H}_2\text{O}$.

In a given solute-solvent contrast, the radius of gyration R_g is a measure of structural elongation if the internal inhomogeneity of scattering densities within the protein has no effect. Guinier analyses at low Q (where $Q = 4\pi \sin \theta/\lambda$; 2θ is the scattering angle and λ is the wavelength) gives the R_g and the forward scattering at zero angle $I(0)$ (27):

$$\ln I(Q) = \ln I(0) - \frac{R_g^2 Q^2}{3}$$

This expression is valid in a $Q.R_g$ range up to 1.5. If the structure is elongated, the mean radius of gyration of cross-sectional structure R_{xs} and the mean cross-sectional intensity at zero angle $[I(Q)Q]_{Q \rightarrow 0}$ is obtained from:

$$\ln[I(Q)Q] = [I(Q)Q]_{Q \rightarrow 0} - \frac{R_{xs}^2 Q^2}{2}$$

The cross-sectional plot for immunoglobulins exhibits two distinct regions, a steeper innermost one and a flatter outermost one (28), identified by R_{xs-1} and R_{xs-2} , respectively. The R_g and R_{xs} analyses were performed using an interactive PERL script program SCTPL7 (J. T. Eaton and S. J. Perkins, unpublished software) on Silicon Graphics OCTANE Workstations. Indirect Fourier transformation of the scattering data $I(Q)$ in reciprocal space into real space to give the distance distribution function $P(r)$ was carried out using the program GNOM (29):

$$P(r) = \frac{1}{2\pi^2} \int_0^\infty I(Q) Q r \sin(Qr) dQ$$

$P(r)$ corresponds to the distribution of distances r between volume elements. This provides the maximum dimension of the antibody L and its most commonly occurring distance vector M in real space. For this, the X-ray $I(Q)$ curve utilized up to 365 data points in the Q range between 0.09 nm^{-1} and 1.70 nm^{-1} . The neutron $I(Q)$ curve utilized up to 45 data points in the Q range between 0.18 nm^{-1} and 1.5 nm^{-1} .

Debye scattering and sedimentation coefficient modelling of IgG1 - A total of 20,000 conformationally randomised human IgG1 models were created by joining the IgG1 Fab and Fc structures with conformationally randomised hinge peptides. The crystal structure of human IgG1 b12 (PDB code 1HZH) was used for this (10). This IgG1 structure has complete heavy chains (H and K) and light chains (L and M), with the exception of thirteen missing K chain residues, namely the Fab $\text{C}_{\text{H}1}$ residues $^{132}\text{SKSTSGG}^{138}$, the core hinge residues $^{223}\text{THT}^{225}$ and the Fc $\text{C}_{\text{H}3}$ C-terminus $^{445}\text{PGK}^{447}$ (10). IgG1 b12 has high sequence identity to IgG1 6a and IgG1 19a (Fig. 2). Most of the sequence differences occur in the V_{H} and V_{L} domains where antigen binding occurs. Additionally, small sequence differences in the $\text{C}_{\text{H}1}$ and $\text{C}_{\text{H}3}$ domains result from allotypic differences. Human IgG1 has four allotypes (G1m1, G1m2, G1m3 and G1m17) which may be expressed in IgG1 as G1m3, G1m17,1 or G1m17,1,2 heavy chains (30). IgG1 b12 is the G1m17,1 allotype with Lys^{214} in the $\text{C}_{\text{H}1}$ domain (Fig. 2D) and Asp^{356} and Leu^{358} in the $\text{C}_{\text{H}3}$ domain (Fig. 2G). Additionally, IgG1 b12 has Ala^{215} in place of the wild type Val^{215} ; this is not an allotypic difference and may have been engineered during the antibody production. IgG1 6a and 19a are both Gm3 allotypes with Arg^{214} in the $\text{C}_{\text{H}1}$ domain (Fig. 2D) and Glu^{356} and Met^{358} in the $\text{C}_{\text{H}3}$ domain (Fig. 2G). The light chain subclass can be either κ or λ . While the κ subclass has only one gene copy, there can be 7-11 gene copies of λ depending on the haplotype (30). The κ light chain subclass has three allotypes (Km1, Km2, Km3), while the λ light chain subclasses have no serologically defined allotypes. The κ light chain allotypes may be expressed as Km1, Km1,2 or Km3.

IgG1 b12, IgG1 6a and IgG1 19a all have the Km3 allotype with Ala¹⁵⁹ and Val¹⁹⁷ in the C_L domain (Fig. 2B). IgG1 b12 shows a sequence difference of Arg²⁰⁸ in the C_L domain (Fig. 2B), which is not an allotypic difference, and may have been engineered. The unhydrated volumes of IgG1 b12, IgG1 6a and IgG1 19a were calculated as 194.3 nm³, 193.1 nm³ and 192.4 nm³ respectively. The volume similarity was within acceptable limits to allow the use of IgG1 b12 as a model for the IgG1 6a and IgG1 19a modelling searches.

In order to generate conformationally randomised trial IgG1 models for scattering fits, four sets of 5,000 models were created, each using different hinges sampled independently at random. Conformational randomisation of the hinges was achieved using molecular dynamics in the Discovery module of the molecular modelling software Insight II (Accelrys) on Silicon Graphics OCTANE workstations. To create the first two sets of asymmetric models, a hinge peptide ²²⁰CDKTHTC²²⁶ was constrained to be of minimum lengths either between 1.72 nm to 2.33 nm, or between 2.33 nm to 2.45 nm (where the latter is almost fully extended in length). As residue Cys²²⁰ is located asymmetrically in relation to the Fc structure, all the created models were asymmetric. Cys²²⁰ and Cys²²⁶ were used as anchor points because they connect the Fab heavy and light chains in a disulphide bridge. To create two more sets of asymmetric and symmetric models, a nineteen-residue hinge peptide ²²⁰CDKTHTCPPCPPELLGGP²³⁸ was constrained with minimum lengths either between 4.66 nm and 6.32 nm, or between 6.32 and 6.65 nm (where the latter is almost fully extended in length) in order to avoid abnormally short hinge structures. As residue Pro²³⁸ was located symmetrically in the Fc structure, the resulting models contained Fab arms in both symmetric and asymmetric orientations about the Fc region. The outermost two residues were anchor points for the superimposition of each hinge conformation onto the Fab and Fc structures in order to create the full IgG1 model.

The X-ray or neutron scattering curve was calculated from each IgG1 model using sphere models for comparison with the experimental IgG1 curves. A cube side of 0.541 nm in

combination with a cut-off of four non-hydrogen atoms was used to convert the atomic coordinates into 1220 spheres that corresponded to the unhydrated structure seen by neutron scattering in ²H₂O. Because hydration shells are visible by X-rays, a hydration shell corresponding to 0.3 g of water per gram of protein was created using HYPRO (31), giving an optimal total of 1607 spheres. The X-ray scattering curve $I(Q)$ was calculated using the Debye equation adapted to spheres (16,32). Steric overlap between the Fab and Fc regions was assessed using the number of spheres n in each model, where models showing less than 95% of the required total of 1607 spheres (X-ray) or 1220 spheres (neutrons) were discarded. Of the 20,000 models, 86% showed no steric overlap. Next, the X-ray R_g , R_{xs-1} and R_{xs-2} values were calculated from the modelled curves in the same Q ranges used for the experimental Guinier fits. Models that passed R_g and R_{xs} filters of $\pm 5\%$ of the experimental value were then ranked using a goodness-of-fit R -factor (defined by analogy with protein crystallography) calculated in the Q range extending to 1.7 nm⁻¹. For the neutron modelling of IgG1 6a, the unhydrated sphere models were used to calculate the scattering curves. Of the 20,000 models, 91% showed no steric overlap. The models created from neutron scattering were assessed as for the X-ray scattering models above, following corrections for wavelength spread and beam divergence, but no correction was required for a flat background caused from incoherent scattering.

Sedimentation coefficients $s_{20,w}^0$ were calculated directly from the hydrated Debye sphere models using the program HYDRO (33). They were also calculated from the atomic coordinates in the HYDROPRO shell modelling program using the default value of 0.31 nm for the atomic element radius for all atoms to represent the hydration shell (34). Previous applications of these calculations to antibodies are reviewed elsewhere (35).

To assess the fit searches, the distances $d1$, $d2$ and $d3$ were determined from the centers-of-mass of the Fab and Fc regions (excluding hydrogen atoms) using a Python script. The three angles between the Fab and Fc regions were defined in a Python script as the angle of intersection from the dot product between two vectors. Each vector was the long axis through

each Fab or Fc region, each defined as the line passing through the centres of gravity between each cluster of four cysteine α -carbon atoms at the two ends of the Fab and Fc regions (one cluster at each end of each Fab or Fc region, corresponding to the conserved disulphide bridge in each immunoglobulin fold domain). Artwork was prepared using PyMOL (Schrödinger, LCC). Superimpositions of the Fc region were performed using the align function within PyMOL. To dock the Fc region with the C1q head, the web server algorithm PatchDock (version beta 1.3) (36) was used in order to take advantage of its ability to include specified residues as potential binding sites. Its output was refined using FireDock from the same web site (37).

Protein Data Bank accession numbers – The three sets of 10 best-fit models are currently available as supplemental material. They have been deposited in the Protein Data Bank under accession codes 4QOU (IgG1 6a by X-rays in PBS-137), 4QOV (IgG1 19a by X-rays in PBS-137) and 4QOW (IgG1 6a by neutrons in PBS-137).

RESULTS

Purification of IgG1 - Both IgG1 6a and IgG1 19a were subjected to gel filtration to ensure that the protein was monodisperse immediately prior to ultracentrifugation or scattering experiments. Both molecules eluted as a symmetric main peak at approximately 15.5 ml (Fig. 3), and showed a single band between 200 and 116 kDa in non-reducing SDS-PAGE that corresponds to the expected masses of 150.1 kDa and 149.7 kDa for intact IgG1 6a and IgG1 19a respectively. Under reducing conditions, the heavy chains for both IgG1 molecules were observed at an apparent molecular mass of 55 kDa, and the light chains were observed between 31 and 21.5 kDa, both as expected (Fig. 3).

Analytical ultracentrifugation of IgG1 - Sedimentation velocity experiments examined the size and shape of IgG1 6a at concentrations between 0.2-4 mg/ml, and IgG1 19a between 0.5-2.24 mg/ml. The SEDFIT analyses involved fits of as many as 745 scans, and the good agreement between the experimental boundary scans and fitted lines is clear (Fig. 4). A major monomer peak was observed at $s_{20,w}$ values of 6.4 S for IgG1 6a and 6.3 S for IgG1

19a. These $s_{20,w}$ values are consistent with the range of values of 6.3–6.8 S previously reported for human IgG1 (38,39,40). Both IgG1 6a and IgG1 19a were predominantly monomeric in solution, and accompanied by a minor dimer peak.

From the $c(s)$ analyses, the molecular masses of the monomer peak for IgG1 6a were reported as 153 kDa (PBS-50), 146 kDa (PBS-137) and 149 kDa (PBS-250) in light water, and 164 kDa (PBS-137 at 20°C) in heavy water. These agree well with the composition-calculated mass of 150 kDa. The molecular mass of the IgG1 19a monomer peak was measured as 161 kDa (PBS-137) in light water, also in agreement with the composition-calculated mass of 150 kDa.

The apparent sedimentation rates of the IgG1 monomer were independent of sample concentration or rotor speed (Fig. 5A). Extrapolation of the corrected $s_{20,w}$ values to zero concentration gave monomer $s_{20,w}^0$ values of 6.42 S for IgG1 6a for 40,000 r.p.m., which is similar to that of 6.44 S for 50,000 rpm (PBS-137 at 20°C). For IgG1 19a, the monomer $s_{20,w}^0$ value was 6.34 S for both rotor speeds of 40,000 and 50,000 rpm (PBS-137 at 20°C). All other data reported in this study are for 40,000 rpm. No change in $s_{20,w}^0$ value was observed at different buffer conditions, with IgG1 6a giving $s_{20,w}^0$ values of 6.42 S, 6.42 S and 6.35 S for PBS-50, PBS-137 and PBS-250 respectively in light water (Fig. 5A). IgG1 6a measured in PBS-137 in heavy water gave an apparent sedimentation of 3.92 S (Fig. 4B). When corrected for the buffer density and viscosity of heavy water, a $s_{20,w}^0$ value of 7.01 S was obtained. Given that the partial specific volume v for proteins is affected by the hydration shell (21,33), and that the hydration shell for heavy water has a higher mass than that for light water, the v values will be reduced in 100% $^2\text{H}_2\text{O}$. When the v value of 0.715 ml/g was used for 20°C in place of 0.728 ml/g, this gave $s_{20,w}^0$ values similar to that of PBS-137 in light water of 6.47 S (Fig. 5A). For IgG1 19a in light water, the $s_{20,w}^0$ value of 6.34 S for PBS-137 at 20°C was similar to that of IgG1 6a. This outcome indicates their similar overall shapes.

The $c(s)$ analyses for IgG1 6a revealed a minor dimer peak at $s_{20,w}^0$ values between 9 S and 10 S in the size-distribution analyses $c(s)$ (Figs. 4 and 5). The molecular masses of the dimer peak

in light water were 263 ± 4 kDa (PBS-50), 260 ± 10 kDa (PBS-137), 257 ± 5 kDa (PBS-250), and 286 ± 9 kDa (PBS-137 in heavy water). These masses are comparable with the expected value of 300 kDa for the IgG1 dimer. The IgG1 6a dimer $s_{20,w}^0$ values in light water were 9.21 ± 0.1 S (PBS-50), 9.69 ± 0.38 S (PBS-137) and 9.12 ± 0.07 S (PBS-250) at 20°C. That in heavy water was similar at 9.35 ± 0.09 S for PBS-137. Similarly, IgG1 19a showed a small dimer peak with a $s_{20,w}^0$ value of 8.8 ± 0.3 S in PBS-137 at 20°C and a molecular mass of 266 ± 9 kDa in light water. This also agreed well with the predicted mass of 300 kDa for its dimer. Integration of the monomer and dimer $c(s)$ peaks showed that the amount of dimer did not alter with sample concentration or buffer composition, with the majority of samples showing less than 5% dimer for both IgG1 6a and IgG1 19a (Fig. 5B).

X-ray and neutron scattering of human IgG1 - The solution structure of IgG1 was jointly analysed by both X-ray and neutron scattering for reason of reproducibility. X-rays in light water buffers monitor the hydration shell as well as the protein structure, while neutrons in heavy water buffers do not see this hydration shell.

X-rays were most effective for looking at IgG1 at 20°C in three different NaCl concentrations. Data collection of IgG1 6a was carried out between 0.5 and 4 mg/ml, using time-frame analyses to ensure the absence of radiation damage effects. Guinier analyses resulted in high-quality linear plots and revealed three distinct regions of the $I(Q)$ curves, as expected for antibodies, from which the R_g , R_{xs-1} and R_{xs-2} values were obtained within satisfactory $Q.R_g$ and $Q.R_{xs}$ limits (Fig. 6A; Table 1). The X-ray R_g values for IgG1 6a in PBS-50, PBS-137 and PBS-250 showed no concentration dependence with mean values of 5.17 nm, 5.19 nm and 5.32 nm respectively (Fig. 7A). There was a slight increase in R_g with salt concentration, most notably with PBS-250. The $I(0)/c$ values for IgG1 6a also showed no concentration dependence (Fig. 7A). Each of the R_{xs-1} and R_{xs-2} values were unchanged between PBS-50, PBS-137 and PBS-250, with a mean R_{xs-1} value of 2.62 nm, 2.64 nm and 2.65 nm, respectively, and a mean R_{xs-2} value of 1.43 nm, 1.43 nm and 1.42 nm, respectively. IgG1 19a was studied between 0.22 and 1.89 mg/ml in the same

buffers as IgG1 6a (Fig. 6C). The X-ray R_g values showed no concentration dependence with mean values of 5.10 nm, 5.22 nm and 5.32 nm in PBS-50, PBS-137 and PBS-250 respectively (Fig. 7C). As for IgG1 6a, there was a slight increase in R_g with increasing NaCl concentration. Similarly, the $I(0)/c$ values for IgG1 19a showed no concentration dependence (Fig. 7C). Each of the R_{xs-1} and R_{xs-2} values were unchanged between PBS-50, PBS-137 and PBS-250, with a mean R_{xs-1} value of 2.63 nm, 2.60 nm and 2.65 nm, respectively, and a mean R_{xs-2} value of 1.48 nm, 1.42 nm and 1.50 nm, respectively (Fig. 7C). The X-ray R_g , $I(0)/c$, R_{xs-1} and R_{xs-2} values for IgG1 19a were in agreement with IgG1 6a.

Neutron scattering viewed the unhydrated protein structure in which the hydration shell is almost invisible in heavy water (33). Neutrons were most useful for temperature studies in PBS-137, as temperature-dependent conditions were less accessible by X-ray scattering. IgG1 6a in 100% $^2\text{H}_2\text{O}$ buffer was analysed between 2.0-4 mg/ml. The Guinier analyses revealed high-quality linear fits for the same three R_g , R_{xs-1} and R_{xs-2} parameters as for X-rays (Fig. 6B). The neutron R_g values remained unchanged with concentration at 6°C, 20°C and 37°C with mean values of 5.18 nm, 5.10 nm and 5.13 nm respectively (Fig. 7B). These R_g values were similar to those for X-ray scattering. The corresponding $I(0)/c$ values also remained unchanged (Fig. 7B). The neutron R_{xs-1} and R_{xs-2} values showed no concentration dependence between 6°C, 20°C and 37°C with mean R_{xs-1} values of 2.48 nm, 2.43 nm and 2.46 nm respectively, and mean R_{xs-2} values of 1.25 nm, 1.25 nm and 1.20 nm, respectively (Fig. 7B). The neutron R_g , R_{xs-1} and R_{xs-2} values were slightly smaller than the corresponding X-ray values, in particular for the two R_{xs} values, and this reduction is attributed primarily to the near invisibility of the surface hydration shell in heavy water, as well as the high negative solute-solvent contrast difference which will also reduce these values (33).

The distance distribution function $P(r)$ provides structural information on IgG1 in real space, namely its overall length and the separation between its Fab and Fc regions. The X-ray $P(r)$ analyses gave R_g values for IgG1 that were similar to those from the X-ray Guinier analyses, showing that the two analyses were

self-consistent (filled and open symbols in Fig. 7A). The maximum length L of IgG1 6a was determined from the value of r when the $P(r)$ curve intersects zero to be 16 nm for PBS-50, PBS-137 and PBS-250 (Fig. 8A). The maxima in the $P(r)$ curves correspond to the most frequently occurring interatomic distances within the structure. For IgG1 6a, two peaks, $M1$ and $M2$, were identified in all the $P(r)$ curves at approximately 4 nm and 7.5 nm respectively. The $M1$ peak corresponds mostly to distances within each Fab and Fc region, while the $M2$ peak corresponds mostly to distances between pairs of Fab and Fc regions. No buffer dependence in the positions of peaks $M1$ and $M2$ was observed (Fig. 9A). Because $M2$ is unchanged, the averaged separation between the Fab and Fc regions within IgG1 remains unchanged in 50-250 mM NaCl. This finding differs from that for IgG4 which showed a concentration dependence of $M2$ below 2 mg/ml (14,15). IgG1 19a showed two $M1$ and $M2$ peaks at similar values of ~ 4 nm and ~ 8 nm respectively (Fig. 9C). IgG1 19a exhibits the same L value of 16 nm as IgG1 6a in PBS-137 and PBS-250. However, the length of IgG1 19a in PBS-50 is slightly reduced at 15 nm (Figs. 8C and 9C).

The neutron $P(r)$ analyses of IgG1 6a in heavy water showed that the R_g values for IgG1 6a at 6°C, 20°C and 37°C did not change with increasing concentration nor temperature (Fig. 7B). The neutron L values were 16 nm at 6°C, 20°C and 37°C (Fig. 8B). The two peaks $M1$ and $M2$ were again identified at approximately 4 nm and 7 nm respectively in the neutron $P(r)$ curves (Fig. 8B). The positions of $M1$ and $M2$ were unchanged with concentration, in agreement with the X-ray $P(r)$ data.

Starting model for the human IgG1 scattering fits - The starting model for scattering fits of IgG1 was the crystal structure of human IgG1 b12 (10). The full hinge is formally defined by the twenty-three residues ²¹⁶EPKSCDKTHTCPPCPAPPELLGGP²³⁸ (3,5) in which the Fab region formally ends at Val²¹⁵ and the Fc region starts at Ser²³⁹ (Fig. 1). The IgG1 hinge contains six Pro residues and two interchain disulphide bridges at Cys²²⁶ and Cys²²⁹. The asymmetric modelling considered only the upper hinge ²²⁰CDKTHTC²²⁶ with Cys²²⁰ and Cys²²⁶ acting as tethers. As this hinge is located asymmetrically relative to the

Fc region, these 10,000 models do not have 2-fold symmetry. Only one of the inter-chain disulphide bonds is intact at Cys²²⁶. The symmetric modelling considered the upper, middle and lower hinge and this resulted in a 19-residue peptide ²²⁰CDKTHTCPPCPAPPELLGGP²³⁸. Because the two Pro²³⁸ residues were located in the middle of the Fc region, this approach generated both symmetric and asymmetric models. For these 10,000 further models, the Cys²²⁶ and Cys²²⁹ inter-chain disulphide bonds were not explicitly intact.

Conformational searches for the human IgG1 solution structure - In order to model both the IgG1 6a and IgG1 19a solution structures, 20,000 conformationally-randomized IgG1 structures were created by connecting the Fab and Fc structures to one of four libraries of conformationally-randomized hinge peptides of lengths 1.72-2.33 nm and 2.33-2.45 nm (asymmetric) and 4.66-6.32 nm and 6.32-6.65 nm (symmetric) (Experimental Procedures). Each modelled scattering curve was compared with the experimental X-ray and neutron scattering curves. To test a broad range of solution conditions, the six modelled X-ray curves were IgG1 6a at the highest available concentrations of 2 mg/ml, 4 mg/ml and 2 mg/ml in PBS-50, PBS-137 and PBS-250 respectively, plus IgG1 19a at the highest available concentrations of 1.4 mg/ml, 1.9 mg/ml and 1.6 mg/ml in PBS-50, PBS-137 and PBS-250 respectively. As previous (15), the occurrence of 4% dimer was assumed to have little effect on the scattering modelling. The modelled neutron curve for IgG1 6a was the highest concentration of 4 mg/ml in PBS-137 at 20°C in heavy water. The seven fit analyses were assessed in R -factor vs. R_g graphs (Fig. 10A-C). In all seven analyses, the occurrence of a single clear minimum in the R -factor values identified a single conformational family of solution structures for IgG1 starting from a wide range of trial orientations and translations of the two Fab and Fc regions. The lowest R -factors in the 20,000 curve fits corresponded to modelled R_g values that were close to the experimental R_g values as desired.

Filters based on the experimental scattering data were used for all 20,000 models to reject unsatisfactory models and identify the ten best-fit models for each search:

(i) A $\pm 5\%$ filter for steric overlap eliminated models in which the Fab and Fc regions sterically overlapped with each other due to inappropriate hinge conformations used in modelling. In order to match the composition-calculated volume of IgG1, sphere models needed a minimum number N of 1607 spheres for the hydrated X-ray models and 1220 spheres for the unhydrated neutron models.

(ii) A $\pm 5\%$ filter for the modelled R_g values (calculated from the same Guinier Q ranges used for the experimental analyses) identified the models that agreed best with the experimental X-ray or neutron R_g values.

(iii) The models that passed the N and R_g filters were arranged in order of their lowest R -factors. The resulting ten best-fit models for IgG1 occurred as a single cluster at the R -factor minimum in each of the seven searches (green in Fig. 10A-C), indicating a single best-fit solution structure.

Only one of the inter-chain disulphide bonds at Cys²²⁶ was conserved in the asymmetric models. For the symmetric models, the pairs of two Cys²²⁶ and two Cys²²⁹ residues may not be proximate in the best-fit models, because the disulphide bridges were not preserved in the libraries. In the ten best-fit models, the α -carbon separations were 0.56-1.49 nm for Cys²²⁶ and 1.14-1.55 nm for Cys²²⁹ in IgG1 6a by X-rays, 0.56-3.63 nm for Cys²²⁶ and 1.55-3.52 nm for Cys²²⁹ in IgG1 19a by X-rays, and 0.56 nm for Cys²²⁶ and 1.55 nm for Cys²²⁹ for IgG1 6a by neutrons. These α -carbon separations were comparable with an expected separation of 0.4-0.75 nm between two bridged Cys residues (41), showing that the best-fit IgG1 models were compatible with disulphide-bridged hinges.

The best-fit modelled curves showed good visual fits in all seven cases with the experimental curves (Fig. 11A-C). In most cases, the R_g values for the ten best-fit models were within error of the experimental values (Table 1). The seven sets of models (Fig. 12A-C) generally displayed asymmetric arrangements of the two Fab regions compared to the Fc region. Both IgG1 6a and IgG1 19a showed mostly asymmetric structures, although a few symmetric structures were observed for IgG1 6a in PBS-137 and IgG1 19a in PBS-250. In summary, both IgG1 6a and IgG1 19a appeared to exhibit a T-shaped arrangement in

PBS-50 and a Y-shaped arrangement in PBS-250 with intermediate T- and Y-shaped structures in PBS-137 (Fig. 12A,C). This shape difference would account for the slightly increased R_g values seen in high salt. Surveys of the distances between the centres of the Fab and Fc regions in the best fit IgG1 6a X-ray and neutron models and IgG1 19a X-ray models showed similar distributions (Fig. 13). The X-ray R -factor values for the best-fit IgG1 models (pink in Fig. 10A,C) were acceptable at 3.0-3.1%, for IgG1 6a and 2.8-3.7% for IgG1 19a (Table 1). The neutron R -factor values were acceptable at 2.6-2.7% (pink in Fig. 10B). These R -factor values compare well with those from other similar modelling fits (35).

Sedimentation coefficient modelling of human IgG1 - The $s_{20,w}^0$ values of the best-fit X-ray hydrated IgG1 models were calculated for comparison with the average experimental values of 6.42 S for IgG1 6a and 6.34 S for IgG1 19a (Fig. 5). For the best-fit hydrated sphere models, the $s_{20,w}^0$ values were 6.67-6.82 S and 6.63-6.90 S for IgG1 6a and IgG1 19a respectively using HYDRO (Table 1). The corresponding $s_{20,w}^0$ values using HYDROPRO were 6.37-6.73 S and 6.37-6.68 S for IgG1 6a and IgG1 19a respectively (Table 1). Given that the calculations should be accurate to within ± 0.21 S (35), the modelled $s_{20,w}^0$ values agree well with the experimental values.

DISCUSSION

The availability of abundant X-ray scattering data for two IgG1 molecules in three buffers permitted a detailed appraisal of the solution structure of human IgG1 and its comparison with the less stable IgG4 solution structure. These experiments were supported by complementary neutron scattering and ultracentrifugation experiments. The data sets enabled atomistic conformational analyses that resulted in seven independent determinations of an asymmetric IgG1 solution structure (Fig. 12A-C). The combination of these IgG1 solution structures with a docking model for the interaction between human IgG1 Fc and the crystal structure of the C1q globular head (42,43), and the crystal structure of the human Fc-Fc γ R receptor (44) show that the Fc region of human IgG1 is exposed and enables this to react readily with its two major effector ligands, unlike human IgG4 (15).

IgG1 has the highest IgG serum concentration of the four IgG subclasses IgG1 to IgG4 at an average level of 8 mg/ml (in a range of 5–12 mg/ml), comprising approximately 60-70 % of the total IgG in normal adult serum (1). IgG1-IgG4 have different heavy chain isotypes which primarily differ in the hinge region (Fig. 2H). IgG1 activates complement-mediated lysis via C1q binding in the complement classical pathway, and binds to all three classes of human Fc γ receptors Fc γ RI, Fc γ RII and Fc γ RIII. IgG1 has different affinities for the Fc γ RI, Fc γ RII and Fc γ RIII, and its binding to different Fc γ Rs on different immune cells result in different immune responses including antibody-dependent cell-mediated cytotoxicity, pro-inflammatory cytokine production and phagocytosis (45). The precise role of the four IgG subclasses in the immune response is unclear. A recent temporal model suggests that the different properties of the IgG subclasses, their concentrations and their emergence at different stages facilitate a more cohesive immune response (46). An understanding of the distinct properties of the IgG subclasses is desired; we now have complete scattering analyses for human IgG1 and IgG4.

Solution structure of human IgG1 6a and IgG1 19a - The two monoclonal IgG1 antibodies studied here have 88.7% total sequence identity, with identical hinge regions and differing primarily in their V_H and V_L domains (Fig. 2). Our X-ray data collection involved the measurement of 52 and 70 curves in two beam sessions (or 520 and 700 curves if time frames are included) (Fig. 7). This abundant data collection enabled the use of different buffers with two different human IgG1. The use of three NaCl concentrations examined potential electrostatic effects on the IgG1 structure, while heavy water is a known promoter of protein self-association. By comparison, earlier scattering studies on human IgG1 reported few scattering and ultracentrifugation runs, or were performed in non-physiological buffer conditions (28,38,39,47-49). Both IgG1 6a and IgG1 19a showed similar experimental R_g and R_{XS} values and the same overall length of 16 nm (Table 1). The two IgG1 molecules also displayed similar experimental $s^0_{20,w}$ values of 6.3-6.4 S, which were indistinguishable within error. The only change with buffer conditions was a small increase in the R_g values in 250 mM NaCl. The 30 best fit structures for IgG1 6a and

IgG1 19a were predominantly asymmetric, with only one symmetric model for IgG1 6a in PBS-137 and two symmetric models for IgG1 19a (PBS-250) (Fig. 12). Little difference was seen between the two IgG1 antibodies. The hinge length is measured by the α -carbon positions of the flanking residues Cys²²⁰ and Pro²³⁸, with a maximum possible length of 6.65 nm. The best-fit structures gave similar hinge lengths of 2.4-5.0 \pm 0.6 nm for IgG1 6a (X-rays), 1.6-5.0 \pm 0.7 nm for IgG1 19a (X-rays), and 3.2-4.9 \pm 0.5 nm for IgG1 6a (neutrons). These lengths show that this hinge is semi-extended. The slight R_g increase in 250 mM NaCl was best explained by a shift from T-shaped structures in low salt to Y-shaped structures in high salt.

The only crystal structure for an intact human IgG is currently that for IgG1 b12 (10), and this structure was used to model the solution scattering data in this study. Two full-length murine IgG crystal structures have also been solved for IgG1 61.1.3 (11) and IgG2a Mab231 (12). These crystal structures only offer a single view of the antibody immobilised in the crystal lattice, in contrast to the expectation that antibodies may display a large range of conformations in solution. Atomistic scattering modelling of the solution structure of IgG1 enhances our understanding of the IgG1 b12 crystal structure and yields the averaged arrangement of the Fab and Fc fragments. IgG1 b12 was crystallised in 800 mM ammonium sulphate and 100 mM sodium cacodylate, pH 6.5. This IgG1 crystal structure showed no symmetry and an asymmetric arrangement of the Fab regions, with one Fab closely packed on top of the Fc region, and the other Fab extended outwards. The two Cys²²⁰-Pro²³⁸ hinge lengths were 3.8 nm and 3.9 nm. Both agree with the modelled hinge lengths for IgG1 6a and IgG1 19a above. The IgG1 b12 R_g , R_{XS-1} and R_{XS-2} values were calculated as 5.12 nm, 2.60 nm and 1.56 nm, in agreement with the values for IgG1 6a and IgG1 19a (Table 1). The IgG1 b12 $s^0_{20,w}$ value was 6.84 S and 6.57 S from HYDRO and HYDROPRO, in agreement with experiment (Table 1). The $d1$, $d2$ and $d3$ values between the Fab and Fc regions were also similar to those for IgG1 6a and IgG1 19a (Fig. 13). It is concluded that the solution structures of IgG1 6a and IgG1 19a are similar to the IgG1 b12 crystal structure.

The comparison of IgG1 6a and IgG1 19a with human IgG4 (15) displayed some differences. Despite similar molecular weights, the R_g values of human IgG1 are 0.1- 0.2 nm larger than those for human IgG4 which has R_g , R_{xs-1} and R_{xs-2} values of 4.92 nm, 2.56 nm and 1.37 nm, respectively. The $s_{20,w}^0$ values of IgG1 6a and IgG1 19a are approximately 0.4 S smaller than IgG4 whose $s_{20,w}^0$ value is 6.8 S (15). Both data sets indicate that IgG1 is more elongated than IgG4. This is attributable to the longer IgG1 hinge sequence, in which the upper hinge contains three extra residues compared to IgG4 (Fig. 2).

Interaction of human IgG1 with C1q - Our atomistic models for intact IgG1 enable the binding of C1q to IgG1 to be assessed. As before, molecular docking of the IgG1 Fc and C1q crystal structures was performed to evaluate this interaction. This structural approach had previously shown that the rabbit IgG interaction with C1q was sterically allowed, but that of human IgG4 with C1q was restricted (15,50). This C1q binding site occurs at the top of the C_{H2} domain in the Fc region near the hinge. Functionally, the reactivity of C1q with the four human IgG subclasses correlates with upper hinge length in the order of IgG3 > IgG1 > IgG2 > IgG4, with IgG4 not activating complement (3). A hingeless IgG1 antibody cannot bind or activate C1q (51). Mutagenesis studies of the hinge modulates C1q binding. These studies include disruption of the inter-heavy chain disulphide covalent bridges in the core hinge that removed the C1q interaction, whereas substitutions in the upper hinge increased C1q binding (52). The mutation of Leu²³⁴ and Leu²³⁵ to Ala residues in the lower hinge of human IgG1 b12 also removed C1q binding, suggesting that the lower hinge is also important (53). A human IgG1 mutant with Thr²²³ and His²²⁴ deleted in the upper hinge, and Pro²²⁷ and Pro²²⁸ deleted in the core hinge cannot bind or activate C1q (52). The isolated IgG4-Fc region binds C1q although intact human IgG4 does not, suggesting that the Fab regions are also important for the C1q interaction (54). In other experiments, the mutation of human IgG1 to mimic the disulphide bonding of IgG4 removed its antibody-dependent cell-mediated cytotoxicity activity (55). Reduction of the inter-heavy chain disulphide bridges showed that these are important for C1q binding (54). Thus the upper,

core and lower hinge contributes to C1q binding and activation, as well as the hinge disulphide bridges.

Docking studies were performed using a shape complementarity method based on the PatchDock server (36) with the best-fit IgG1 6a and IgG1 19a models (Fig. 14A,B). Human IgG1 residues involved in C1q binding include Asp²⁷⁰, Lys³²², Pro³²⁹ and Pro³³¹ in the Fc C_{H2} region (56,57). Docking and molecular dynamic simulations identified 19 C1q and 12 Fc contact residues in the IgG1-C1q complex (Table 2 of (43)). Using these residues to guide the docking, both Fab regions in both IgG1 6a and IgG1 19a were seen to be positioned away from the C1q binding site, hence enabling C1q to bind. Steric clashes between the docked IgG1-C1q complexes were evaluated, and compared with those for docked IgG4-C1q models (Fig. 15). The globular C1q head has a molecular weight of 44.1 kDa and an unhydrated volume of 57.1 nm³ (21). Residues making main-chain clashes were identified using Swiss-PdbViewer (58), and their amino acid volumes were summed to estimate a notional C1q volume obstructed by the Fab-arms. Based on all the best-fit structures, the mean obstructed volume for IgG1 6a-C1q was 6.9 nm³, that for IgG1 19a-C1q was 2.1 nm³ and that for IgG4-C1q was 19.1 nm³. This comparison showed that the IgG4 Fab regions hindered C1q binding by about 3-9 times the volume than the IgG1 Fab regions. Given that there are two identical C1q binding sites on either side of the Fc region, visual inspection revealed that the other C1q binding site is obstructed in both IgG1 and IgG4 structures. IgG constructs with one half binding C1q and one half not binding C1q were still able to bind C1q, indicating that 1:1 stoichiometry of Fc:C1q is possible (59). Therefore the accessibility of only one C1q binding site in IgG1 is adequate for complement activation.

Sequence differences between the IgG subclasses may also account for the reduced binding of C1q, with Pro³²⁹ and Pro³³¹ likely to be important for this (60,61). The strength of Fc-C1q binding is not directly correlated to complement activation, with IgG1 better able to activate complement-mediated lysis than IgG3, despite the stronger binding of IgG3 to C1q, for example (62). This suggests that binding of C1q alone is not enough to activate the complement

cascade. The Fc-C1q affinity is low with a dissociation constant K_D of approximately 10^4 M (63,64). Localised IgG clusters may bind a C1q hexamer through multivalent contacts to increase the strength of the C1q-Fc interaction, as exemplified by a hexamer configuration of an IgG1 mutant (65).

Interaction of human IgG1 with FcγR – FcγR receptors are present on immune cell surfaces, and are divided into low-affinity (subclasses FcγRIIA/B/C and FcγRIIIA/B) and high-affinity (subclass FcγRI only) types. Both FcγR types bind IgG immune complexes, but only the high-affinity FcγR bind monomeric IgG as well. The binding of therapeutic antibodies to native FcγR *in vivo* is sometimes exploited to produce drug action. The affinities of the four human IgG subclasses for specific FcγRs vary due to the presence of different contact residues in the Fc fragment and the FcγRs. Human IgG1 and IgG3 binds to all the Fcγ receptors (FcγRI, FcγRIIA, FcγRIIB/C, FcγRIIIA, FcγRIIIB) whereas IgG2 and IgG4 only bind to some of them. For FcγRI, IgG1 and IgG3 bind most strongly (K_A 6.5 and 6.1×10^7 M⁻¹ respectively), IgG4 binding is slightly weaker (3.4×10^7 M⁻¹), and IgG2 displayed no measurable binding. For the remaining FcγRII and FcγRIII subclasses, IgG1 and IgG3 bound to all the FcγRII and FcγRIII receptors with high K_A values ranging between 1.2×10^5 M⁻¹ to 9.8×10^6 M⁻¹. In contrast, IgG4 showed low affinity binding with K_A values in the region of 2×10^7 M⁻¹ for FcγRIIA/B/C and no measurable binding to FcγRIIIB. IgG2 showed mostly lower affinities than IgG1, IgG3 and IgG4 for all FcγRs, including no measurable binding for FcγRIIIB (45).

Our atomistic models for intact IgG1 enable the binding of FcγR to intact IgG1 to be reviewed. Crystal structures of the IgG1 Fc-FcγRIIIB complex show that FcγR binds to the top of the Fc region close to the hinge (44,66). The feasibility of the IgG1-FcγR interaction in full-length IgG1 was revealed by superimposition of our best fit IgG1 6a and IgG1 19a structures with the IgG1 Fc-FcγRIIIB crystal structure (44). FcγR binding is seen to be permitted because the Fab regions in our IgG1 models do not sterically clash with FcγR (Fig. 14C,D). This is in contrast to the blocked human IgG4-FcγRIIIB interaction (15) (Fig. 15). Other factors affecting the strength of Fc-FcγR

binding include residues present in the hinge and C_H2 domains. The IgG1 Fc residues associated with FcγR binding include ²³⁴LLGGP²³⁸ of the lower hinge region (67) and ²⁶⁵DVSHE²⁶⁹, ²⁹⁷NST²⁹⁹ and ³²⁹PAPIE³³³ of the C_H2 domain (Fig. 2) (68,44,53). Hinge mutagenesis studies revealed that disrupting the core hinge (CPPCP; Fig. 2) leads to reduced IgG1 binding to FcγRIIIA (52). Sequence differences in the IgG subclass heavy chains may also be relevant, with IgG1 and IgG3 possesses Leu²³⁴ and Leu²³⁵ in the lower hinge region, whereas IgG2 has Val²³⁴ and Ala²³⁵, and IgG4 has a Phe²³⁴ (Fig. 2). IgG4 also has Ser³³⁰ and Ser³³¹ substitutions compared to the other IgG subclasses (68,61). These substitutions in IgG2 and IgG4 lead to weaker FcγR binding in comparison to IgG1 and IgG3 which bind to all FcγR classes.

Steric clashes between the docked IgG1-FcγR complexes were also evaluated, and compared with those for the IgG4-FcγR models. The crystal structure of a human IgG1-Fc with the human FcRIII extracellular domains, which have a molecular weight of 20.1 kDa and an unhydrated volume of 25.8 nm³ (21). As with the IgG-C1q models above, residues making main-chain clashes were identified using Swiss-PdbViewer (58), and their amino acid volumes were summed to estimate a notional FcγR volume obstructed by the Fab-arms. Based on all the best-fit structures, the mean obstructed volume for IgG1 6a-FcγR was 6.6 nm³, that for IgG1 19a-FcγR was 1.6 nm³ and that for IgG4-FcγR was 14.8 nm³. This comparison showed that the IgG4 Fab regions hindered FcγR binding by about 3-9 times the volume than the IgG1 Fab regions.

Stability of human IgG1 - Antibody stability is a major concern in the context of the multibillion antibody industry where stabilities may be compromised during manufacturing, shipping and storage (69). The conformational stability of IgG1 is important, as changes in the native structure may lead to aggregation or self-association (70). The stability of human IgG1 6a and IgG1 19a was explored here using different buffers and temperatures. Their R_g values increased slightly with increasing salt concentration (Fig. 7), indicating more elongated structures arise in higher salt concentrations from changes in the electrostatic interactions between surface amino acid

residues. However, no changes were revealed by the $M1$ and $M2$ values or $s_{20,w}^0$ values (Figs. 7 and 9). No temperature dependence was observed for IgG1 6a by neutron scattering, with no changes in R_g and R_{xs} , and no movement of the $M1$ and $M2$ peaks (Figs. 8 and 9). In marked contrast to IgG1, human IgG4 displays conformational instabilities in the $P(r)$ curves below 2 mg/ml, these being attributable to different diffusion-collision events at different concentrations, or to the occurrence of Fab-arm exchange in dilute IgG4 concentrations (14,15). Human IgG1 also showed no significant concentration-dependent dimerization by neutron scattering in heavy water, unlike the noticeable dimer formation seen for IgG4.

IgG1 aggregation and self-association are relevant also to the immune response *in vivo* as well as in treatments with therapeutic antibodies. Human serum naturally contains a total of 1% dimeric IgG1, with less than 0.03% of this being covalent IgG1 dimers (71). Different oligomeric forms of human IgG1 could enhance the binding to FcγRs and C1q through their increased avidity as expected (65,72). IgG1 dimers are found in therapeutic drugs such as Epratuzumab (73), which is currently in clinical trials, and Food and Drug Administration-approved Palivizumab (74).

The presence of dimers and/or aggregates in preparations of therapeutic antibodies is usually below 1% and is regarded as an impurity (i.e. not mediating the desired pharmacological effect). Assessing the aggregation profile of antibody pharmaceuticals is crucial as any aggregates may affect its efficacy and immunogenicity. The low amounts below 5% of IgG1 dimer observed by sedimentation velocity in four different buffers (Figs. 4 and 5) showed that IgG1 6a and IgG1 19a do not undergo significant buffer- or concentration-dependent dimerization under the conditions tested, especially in heavy water which promotes self-association. The dimer peak has an $s_{20,w}^0$ value of about 9.5 S (Fig. 5), similar to that of the rabbit IgG dimer, suggesting that this dimer may be relatively compact in its structure (50). Antibodies may dimerise through the association of their Fab-Fab and Fab-Fc regions (74), although that for rabbit IgG was attributed to the formation of Fab-Fab pairs (50).

Acknowledgements - We thank Dr Bryan Smith (UCB) for generously providing human IgG1 6a and IgG1 19a. We thank Dr T. Narayanan at the ESRF in Grenoble and Dr Sarah Rogers at ISIS for excellent instrumental support.

REFERENCES

1. Hamilton, R. G. (2001) The Human IgG Subclasses, Calbiochem Corporation http://www.antibodybeyond.com/books/Calbiochem_Human_IgG_Booklet_CB0051.pdf.
2. Strohl, W. R. and Strohl, L. M. (2012) *Therapeutic antibody engineering: current and future advances driving the strongest growth area in the pharmaceutical industry*. Woodland Publishing Ltd, Cambridge, UK.
3. Dangl, J. L., Wensel, T. G., Morrison, S. L., Stryer, L., Herzenberg, L. A. and Oi, V. T. (1988) Segmental flexibility and complement fixation of genetically engineered chimeric human, rabbit and mouse antibodies. *EMBO J.* **7**, 1989-1994.
4. Roux, K. H., Strelets, L. and Michaelsen, T. E. (1997) Flexibility of human IgG subclasses. *J. Immunol.* **159**, 3372-3382.
5. Brekke, O. H., Michaelsen, T. E. and Sandlie, I. (1995) The structural requirements for complement activation by IgG: does it hinge on the hinge? *Immunol. Today*, **16**, 85-90.
6. Lund, J., Winter, G., Jones, P. T., Pound, J. D., Tanaka, T., Walker, M. R., Artymiuk, P. J., Arata, Y., Burton, D. R., Jefferis, R. and Woof, J. M. (1991) Human FcγRI and FcγRII interact with distinct but overlapping sites on human IgG. *J. Immunol.* **147**, 2657-2662.
7. Sarma, R. and Laudin, A. G. (1982) The three-dimensional structure of a human IgG1 immunoglobulin at 4Å resolution: a computer fit of various structural domains on the electron density map. *J. Appl. Cryst.* **15**, 476-481.
8. Marquart, M., Deisenhofer, J. and Huber, R. (1980) Crystallographic refinement and atomic models of the intact immunoglobulin molecule Kol and its antigen-binding fragment at 3.0Å and 1.9Å resolution. *J. Mol. Biol.* **141**, 369-391.

9. Guddat, L. W., Herron, J. N. and Edmundson, A. B. (1993) Three-dimensional structure of a human immunoglobulin with a hinge deletion. *Proc. Natl. Acad. Sci. U.S.A.* **90**, 4271-4275.
10. Saphire, E. O., Parren, P. W., Pantophlet, R., Zwick, M. B., Morris, G. M., Rudd, P. M., Dwek, R. A., Stanfield, R. L., Burton, D. R. and Wilson, I. A. (2001) Crystal structure of a neutralizing human IgG against HIV-1: a template for vaccine design. *Science*, **293**, 1155-1159.
11. Harris, L. J., Skaletsky, E. and McPherson, A. (1998) Crystallographic structure of an intact IgG1 monoclonal antibody. *J. Mol. Biol.* **275**, 861-872.
12. Harris, L. J., Larson, S. B., Hasel, K. W. and McPherson, A. (1997) Refined structure of an intact IgG2a monoclonal antibody. *Biochemistry*, **36**, 1581-1597.
13. Saphire, E. O., Stanfield, R. L., Crispin, M. D. M., Parren, P. W. H. I., Rudd, P. M., Dwek, R. A., Burton, D. R. and Wilson, I. A. (2002) Contrasting IgG structures reveal extreme asymmetry and flexibility. *J. Mol. Biol.* **319**, 9-18.
14. Abe, Y., Gor, J., Bracewell, D. G., Perkins, S. J. and Dalby, P. A. (2010) Masking of the Fc region is human IgG4 by constrained X-ray scattering modelling: implications for antibody function and therapy. *Biochem. J.* **432**, 101-111.
15. Rayner, L. E., Hui, G. K., Gor, J., Heenan, R. K., Dalby, P. A. and Perkins, S. J. (2014) The Fab conformations in the solution structure of human IgG4 restricts access to its Fc region: implications for functional activity. *J. Biol. Chem.* **289**, 20740-20756.
16. Boehm, M. K., Woof, J. M., Kerr, M. A. and Perkins, S. J. (1999) The Fab and Fc fragments of IgA1 exhibit a different arrangement from that in IgG: a study by X-ray and neutron solution scattering and homology modelling. *J. Mol. Biol.* **286**, 1421-1447.
17. Furtado, P. B., Whitty, P. W., Robertson, A., Eaton, J. T., Almogren, A., Kerr, M. A., Woof, J. M. and Perkins, S. J. (2004) Solution structure determination of monomeric human IgA2 by X-ray and neutron scattering, analytical ultracentrifugation and constrained modelling: A comparison with monomeric human IgA1. *J. Mol. Biol.* **338**, 921-941.
18. Sun, Z., Almogren, A., Furtado, P. B., Chowdhury, B., Kerr, M. A. and Perkins, S. J. (2005) Semi-extended solution structure of human myeloma immunoglobulin D determined by constrained X-ray scattering. *J. Mol. Biol.* **353**, 155-173.
19. Perkins, S. J., Nealis, A. S., Sutton, B. J. and Feinstein, A. (1991) Solution structure of human and mouse immunoglobulin M by synchrotron X-ray scattering and molecular graphics modelling. *J. Mol. Biol.* **221**, 1345-1366.
20. Deisenhofer, J. (1981) Crystallographic refinement and atomic models of a human Fc fragment and its complex with fragment B of protein A from *Staphylococcus aureus* at 2.9- and 2.8-Å resolution. *Biochemistry*, **20**, 2361-2370.
21. Perkins, S. J. (1986) Protein volumes and hydration effects: the calculation of partial specific volumes, neutron scattering matchpoints and 280-nm absorption coefficients for proteins and glycoproteins from amino acid sequences. *Eur. J. Biochem.* **157**, 169-180.
22. Laue, T. M., Shah, B. D., Ridgeway, T. M. and Pelletier, S. L. (1992) Computer-aided interpretation of analytical sedimentation data for proteins. In *Analytical Ultracentrifugation in Biochemistry and Polymer Science* (Harding, S. E., Rowe, A. J. and Horton, J. C., eds), pp. 90-125, The Royal Society of Chemistry, Cambridge, U.K.
23. Schuck, P. (1998) Sedimentation analysis of non-interacting and self-associating solutes using numerical solutions to the Lamm equation. *Biophys. J.* **75**, 1503-1512.
24. Schuck, P. (2000) Size-distribution analysis of macromolecules by sedimentation velocity ultracentrifugation and Lamm equation modelling. *Biophys. J.* **78**, 1606-1619.
25. Narayanan, T., Diat, O. and Bösecke, P. (2001) SAXS and USAXS on the high brilliance beamline at the ESRF. *Nucl. Instrum. Methods Phys. Res. Section A*, **467-468**, 1005-1009.
26. Heenan, R. K., Rogers, S. E., Turner, D., Terry, A. E., Treadgold, J. and King, S. M. (2011) Small angle neutron scattering using Sans2d. *Neutron News*, **22**, 19-21.
27. Glatter, O. and Kratky, O. (1982) *Small angle X-ray scattering*, Academic Press, New York.
28. Pilz, I., Kratky, O., Licht, A. and Sela, M. (1973) Shape and volume of anti-poly(D-alanyl) antibodies in the presence and absence of tetra-D-alanine as followed by small-angle X-ray scattering. *Biochemistry* **12**, 4998-5005.
29. Semenyuk, A. V. and Svergun, D. I. (1991) GNOM – a program package for small-angle scattering data-processing. *J. Appl. Crystallogr.* **24**, 537-540.

30. Jefferis, R. and Lefranc, M. P. (2009) Human immunoglobulin allotypes: possible implications for immunogenicity. *MAbs*, **1**, 332-338.
31. Ashton, A. W., Boehm, M. K., Gallimore, J. R., Pepys, M. B. and Perkins, S. J. (1997) Pentameric and decameric structures in solution of the serum amyloid P component by X-ray and neutron scattering and molecular modelling analyses. *J. Mol. Biol.* **272**, 408-422.
32. Perkins, S. J. (2001) X-ray and neutron scattering analyses of hydration shells: a molecular interpretation based on sequence predictions and modelling fits. *Biophys. Chem.* **93**, 129-139.
33. Garcia de la Torre, J., Navarro, S., Lopez Martinez, M. C., Diaz, F. G. and Lopez Cascales, J. (1994) HYDRO: a computer program for the prediction of hydrodynamic properties of macromolecules. *Biophys. J.* **67**, 530-531.
34. Garcia de la Torre, J., Huertas, M. L. and Carrasco, B. (2000) Calculation of hydrodynamic properties of globular proteins from their atomic-level structure. *Biophys. J.* **78**, 719-730.
35. Perkins, S. J., Okemefuna, A. I., Nan, R., Li, K. and Bonner, A. (2009) Constrained solution scattering modelling of human antibodies and complement proteins reveals novel biological insights. *J. R. Soc. Interface*, **6**, S679-696.
36. Schneidman-Duhovny, D., Inbar, Y., Nussinov, R. and Wolfson, H. J. (2005) PatchDock and SymmDock: servers for rigid and symmetric docking. *Nucleic Acids Res.* **33**, W363-W367.
37. Andrusier, N., Nussinov, R. and Wolfson, H. J. (2007) FireDock: Fast Interaction Refinement in Molecular Docking. *Proteins*, **69**, 139-159.
38. Kilár, F., Simon, I., Lakatos, S., Vonderviszt, F., Medgyesi, G. A. and Závodszy, P. (1985) Conformation of human IgG subclasses in solution. Small-angle X-ray scattering and hydrodynamic studies. *Eur. J. Biochem.* **147**, 17-25.
39. Gregory, L., Davis, K. G., Sheth, B., Boyd, J., Jefferis, R., Nave, C. and Burton, D. R. (1987) The solution conformations of the subclasses of human IgG deduced from sedimentation and small angle X-ray scattering studies. *Mol. Immunol.* **24**, 821-829.
40. Phillips, M. L., Tao, M. H., Morrison, S. L. and Schumaker, V. N. (1994) Human/mouse chimeric monoclonal antibodies with human IgG1, IgG2, IgG3 and IgG4 constant domains: electron microscopic and hydrodynamic characterization. *Mol. Immunol.* **31**, 1201-10.
41. Richardson, J. S. and Richardson, D. C. (1989) Principles and patterns of protein conformation. In *Prediction of Protein Structure and the Principles of Protein Conformation* (Fasman, G. D., ed.), pp. 1-98, Plenum Press, New York, NY.
42. Gaboriaud, C., Juanhuix, J., Gruez, A., Lacroix, M., Darnault, C., Pignol, D., Verger, D., Fontecilla-Camps, J. C. and Arlaud, G. (2003) The crystal structure of globular head of complement protein C1q provides a basis for its versatile recognition properties. *J. Biol. Chem.* **278**, 46974-46982.
43. Schneider, S. and Zacharias, W. (2012) Atomic resolution model of the antibody Fc interaction with the complement C1q component. *Mol. Immunol.* **51**, 66-72.
44. Sondermann, P., Huber, R., Oosthuizen, V. and Jacob, U. (2000) The 3.2 Å crystal structure of the human IgG1 Fc fragment-FcγRIII complex. *Nature*, **406**, 267-273.
45. Bruhns, P., Iannascoli, B., England, P., Mancardi, D. A., Fernandez, N., Jorieux, S. and Daëron, M. (2009) Specificity and affinity of human Fcγ receptors and their polymorphic variants for human IgG subclasses. *Blood*, **113**, 3716-3725.
46. Collins, A. M. and Jackson, K. J. L. (2013) A temporal model of human IgE and IgG antibody function. *Frontiers in Immunology*, **4**, 1-6.
47. Calmettes, P., Cser, L. and Rajnavölgyi, É. (1991) Temperature and pH dependence of immunoglobulin G conformation. *Arch. Biochem. Biophys.* **291**, 277-283.
48. Ashish, Solanki, A. K., Boone, C. D. and Krueger, J. K. (2010) Global structure of HIV-1 neutralizing antibody IgG1 b12 is asymmetric. *Biochem. Biophys. Res. Commun.* **391**, 947-951.
49. Lilyestrom, W. G., Shire, S. J. and Scherer, T. M. (2012) Influence of the cosolute environment on IgG solution structure analyzed by small-angle X-ray scattering. *J. Phys. Chem. B*, **116**, 9611-9618.
50. Rayner, L. E., Kadkhodayi-Kholghi, N., Heenan, R. K., Gor, J., Dalby, P. A. and Perkins, S. J. (2013) The solution structure of rabbit IgG accounts for its interactions with the Fc receptor and complement C1q and its conformational stability. *J. Mol. Biol.* **425**, 506-523.

51. Klein, M., Haeffner-Cavaillon, N., Isenman, D. E., Rivat, C., Navia, M. A., Davies, D. R. and Dorrington, K. J. (1981) Expression of biological effector functions by immunoglobulin G molecules lacking the hinge region. *Proc. Natl. Acad. Sci. U.S.A.* **78**, 524-528.
52. Dall'Acqua, W. F., Cook, K. E., Damschroder, M. M., Woods, R. M. and Wu, H. (2006) Modulation of the effector functions of a human IgG1 through engineering of its hinge region. *J. Immunol.* **177**, 1129-1138.
53. Hezareh, M., Hessel, A. J., Jensen, R. C., van de Winkel, J. G. and Parren, P. W. (2001) Effector function activities of a panel of mutants of a broadly neutralizing antibody against human immunodeficiency virus type 1. *J. Virol.* **75**, 12161-12168.
54. Isenman, D. E., Dorrington, K. J. and Painter, R. H. (1975) The structure and function of immunoglobulin domains. *J. Immunol.* **114**, 1726-1729.
55. Dorai, H., Wesolowski, J. S. and Gillies, S. D. (1992) Role of the inter-heavy and light chain disulfide bonds in the effector functions of human immunoglobulin IgG1. *Mol. Immunol.* **29**, 1487-1491.
56. Idusogie, E. E., Presta, L. G., Gazzano-Santoro, H., Totpal, K., Wong, P. Y., Ultsch, M., Meng, Y. G. and Mulkerrin, M. G. (2000) Mapping of the C1q binding site on Rituxan, a chimeric antibody with human IgG1 Fc. *J. Immunol.* **164**, 4178-4184.
57. Thommesen, J. E., Michaelsen, T. E., Loset, G. A., Sandlie, I and Brekke, O. H. (2000) Lysine 322 in the human IgG3 CH2 domain is crucial for antibody dependent complement activation. *Mol. Immunol.* **37**, 995-1004.
58. Guex, N. and Peitsch, M. C. (1997) SWISS-MODEL and the Swiss-PdbViewer: An environment for comparative protein modelling. *Electrophoresis*, **18**, 2714-2723.
59. Michaelsen, T. E., Thommesen, J. E., Ihle, O., Gregers, T. F., Sandin, R. H., Brekke, O. H. and Sandlie, I. (2006) A mutant human IgG molecule with only one C1q binding site can activate complement and induce lysis of target cells. *European Journal of Immunology*, **36**, 129-138.
60. Tao, M. H., Smith, R. I. F. and Morrison, S. L. (1993) Structural features of human immunoglobulin G that determine isotype-specific differences in complement activation. *J. Exp. Med.* **178**, 661-667.
61. Davies, A. M., Rispens, T., Ooijselaar-de Heer, P., Gould, H. J., Jefferis, R., Aalberse, R. C. and Sutton, B. J. (2014) Structural determinants of unique properties of human IgG4-Fc. *J. Mol. Biol.* **426**, 630-644.
62. Brüggemann, M., Williams, G. T., Bindon, C. I., Clark, M. R., Walker, M. R., Jefferis, R., Waldmann, H. and Neuberger, M. S. (1987) Comparison of the effector functions of human immunoglobulins using a matched set of chimeric antibodies. *J. Exp. Med.* **166**, 1351-1361.
63. Hughes-Jones, N. C. and Gardner, B. (1979) Reaction between the isolated globular sub-units of the complement component C1q and IgG-complexes. *Mol. Immunol.*, **16**, 697-701.
64. Feinstein, A., Richardson, N. and Taussig, M. I. (1986) Immunoglobulin flexibility in complement activation. *Immunology Today*, **7**, 169-174.
65. Diebold, C. A., Beurskens, F. J., de Jong, R. N., Koning, R. I., Strumane, K., Lindorfer, M. A., Voorhorst, M., Ugurlar, D., Rosati, S., Heck, A. J. R., van de Winkel, J. G. J., Wilson, I. A., Koster, A. J., Taylor, R. P., Saphire, E. O., Burton, D. R., Schuurman, J., Gros, P. and Parren, P. W. H. I. (2014) Complement is activated by IgG hexamers assembled at the cell surface. *Science*, **343**, 1260-1263.
66. Radaev, S., Motykai, S., Fridman, W. H., Sautes-Fridman, C. and Sun, P. D. (2001) The structure of a human type III Fcγ receptor in complex with Fc. *J. Biol. Chem.* **276**, 16469-16477.
67. Tamm, A. and Schmidt, R. E. (1997) IgG binding sites of human Fcγ receptors. *Intern. Rev. Immunol.* **16**, 57-85.
68. Radaev, S. and Sun, P. (2001) Recognition of immunoglobulins by Fcγ receptors. *Mol. Immunol.* **38**, 1073-1083.
69. Wang, W., Singh, S., Zeng, D. L., King, K. and Nema, S. (2007) Antibody structure, instability and formulation. *J. Pharm. Sci.* **96**, 1-26.
70. Manning, M. C., Chou, D. K., Murphy, B. M., Payne, R. W. and Katayama, D. S. (2010) Stability of protein pharmaceuticals: an update. *Pharm. Res.* **27**, 544-575.
71. Yang, J., Goetze, A. M. and Flynn, G. C. (2014) Assessment of naturally occurring covalent and total dimer levels in human IgG1 and IgG2. *Mol. Immunol.* **58**, 108-115.

72. Luo, Y., Lu, Z., Raso, S. W., Entrican, C. and Tangarone, B. (2009) Dimers and multimers of monoclonal IgG1 exhibit higher in vitro binding affinities to Fc γ receptors. *mAbs*, **1**, 491-504.
73. Remmele, R. L. Jr, Callahan, W. J., Krishnan, S., Zhou, L., Bondarenko, P. V., Nichols, A. C., Kleemann, G. R., Pipes, G. D., Park, S., Fodor, S., Kras, E. and Brems, D. N. (2006) Active dimer of Epratuzumab provides insight into the complex nature of an antibody aggregate. *J. Pharm. Sci.* **95**, 126-145.
74. Iwura, T., Fukuda, J., Yamazaki, K., Kanamaru, S. and Arisaka, F. (2014) Intermolecular interactions and conformations of antibody dimers present in IgG1 biopharmaceuticals. *J. Biochem.* **155**, 63-71.

FOOTNOTES

This work was supported by the Biotechnology and Biological Sciences Research Council. Support for this work was also provided in part by the CCP-SAS project, a joint EPSRC (EP/K039121/1) and NSF (CHE-1265821) grant.

The abbreviations used are: FcR, Fc receptor; IgG, immunoglobulin G.

FIGURE LEGENDS

FIGURE 1. The human IgG1 domain structure. The heavy chains have V_H, C_{H1}, C_{H2} and C_{H3} domains, and the light chains have V_L and C_L domains. The heavy chains are connected by two Cys–Cys disulphide bridges at Cys²²⁶ and Cys²²⁹. There is one N-linked oligosaccharide site at Asn²⁹⁷ on each of the C_{H2} domains. The hinge region between the Fab and Fc fragments is composed of 23 residues (EPKSCDKTHTCPPCPAPELLGGP) between Val²¹⁵ and Ser²³⁹.

FIGURE 2. Sequence alignment of human IgG1. The IgG1 6a and 19a sequences were kindly provided by Dr Bryan Smith at UCB. The IgG1 b12 sequence was taken from its crystal structure (PDB code 1HZH). *A,B*, The V_L and C_L domains. *C-E*, the V_H and C_{H1} domains and the hinge. *F,G*, the C_{H2} and C_{H3} domains. *H*, comparison of the hinge sequences from the human IgG subclasses and rabbit IgG. For the V_L, C_L and V_H domains, consecutive sequence numbering was used. For the C_{H1}, C_{H2} and C_{H3} domains, EU sequence numbering was used.

FIGURE 3. Purification of human IgG1. *A*, IgG1 6a and *B*, IgG1 19a. For each antibody, the elution peak from a Superose 6 10/300 gel filtration column is shown on the left (mAU, milli-absorbance units) with molecular weight markers (kDa). The non-reduced and reduced SDS-PAGE analyses are shown on the right.

FIGURE 4. Sedimentation velocity analyses of IgG1. The experimentally observed sedimentation boundaries for IgG1 6a in *A* PBS-50, PBS-137, PBS-250 in H₂O and *B* PBS-137 in ²H₂O buffers were recorded at a rotor speed of 40,000 r.p.m. and 20°C. *C* IgG1 19a in PBS-137 at 20°C was also measured at 40,000 r.p.m.. Forty boundaries (black outlines) are shown from up to 745 scans at intervals of every *e.g.* 15th scan for clarity which were fitted using SEDFIT as shown (white lines). The right panel shows the observed *s* values in the corresponding size-distribution analyses *c(s)* revealing a monomer (M) peak at *s*_{20,w}⁰ values of approximately 6.4 S for IgG1 6a and 6.3 S for IgG1 19a in H₂O buffers, with a minor dimer peak (D) at about 9 S. The observed *s* values in ²H₂O buffers are shifted to lower *s* values.

FIGURE 5. Summary of IgG1 sedimentation analyses. *A*, the *s*_{20,w} values for the monomer and dimer peaks are shown as a function of IgG1 concentration in five buffers. *B*, the percentages of monomer and dimer from integration of the *c(s)* analyses. For IgG1 6a, four buffers are denoted as PBS-50 (□), PBS-137 (○) and PBS-250 (◇) in H₂O at 20°C and in PBS-137 in ²H₂O at 20°C (●). For IgG1 19a, PBS-137 at 20°C is shown as ★. For IgG1 6a, the average *s*_{20,w} values of monomer and dimer and their integrations are shown for PBS-50 (⋯), PBS-137 (- -) and PBS-250 (—) buffers in H₂O at 20°C and in PBS-137 (²H₂O) buffer at 20°C (- · -). For IgG1 19a, those for PBS-137 at 20°C (- · -) is shown.

FIGURE 6. X-ray and neutron Guinier *R_g* and *R_{xs}* analyses for IgG1.

A, the X-ray scattering curves of IgG1 6a are shown for concentrations of 0.5, 1, 1.5 and 2 mg/ml from bottom to top in three buffers PBS-50, PBS-137 and PBS-250 at 20°C. In PBS-137, an additional scattering curve for 4.0 mg/ml is displayed. The filled circles represent the Q , R_g and Q , R_{XS} ranges used to determine the R_g and R_{XS} values. The Q -ranges used for the R_g values in PBS-50 and PBS-137 was 0.09-0.28 nm⁻¹ with the exception of 1 mg/ml IgG1 6a in PBS-50 which was 0.15-0.28 nm⁻¹. The Q -range used for the R_g values in PBS-250 was 0.15-0.28 nm⁻¹. The R_{XS-1} and R_{XS-2} Q -ranges were 0.31-0.47 nm⁻¹ and 0.65-1.04 nm⁻¹ respectively.

B, the neutron scattering curves of IgG1 6a are shown for concentrations of 2, 3 and 4 mg/ml from bottom to top for IgG1 in PBS-137 (²H₂O) at 6°C, 20°C and 37°C. The Q range used for the R_g values was 0.18–0.28 nm⁻¹ and those for the R_{XS-1} and R_{XS-2} values were 0.31–0.47 nm⁻¹ and 0.65–1.04 nm⁻¹, respectively.

C, the X-ray scattering curves of IgG1 19a for concentrations of 0.22, 0.34, 0.45, 0.68, 0.90 and 1.35 mg/ml in PBS-50 buffer, 0.30, 0.47, 0.62, 0.95, 1.27 and 1.89 mg/ml in PBS-137 buffer and at 0.26, 0.41, 0.81 and 1.62 mg/ml in PBS-250 buffer at 20°C from bottom to top. The Q range used for the R_g values was 0.09–0.28 nm⁻¹ for PBS-50 and PBS-137 buffers whereas a Q range of 0.15-0.28 was used for PBS-250 buffer. The R_{XS-1} and R_{XS-2} Q -ranges were 0.31–0.47 nm⁻¹ and 0.65–1.04 nm⁻¹, respectively.

FIGURE 7. Concentration and temperature dependence of the X-ray and neutron Guinier analyses. The Guinier analyses are shown in Fig. 6. The open symbols show the values from the Guinier analyses, and the filled symbols show those from the $P(r)$ analyses. A, C, the X-ray values for IgG1 6a and IgG1 19a respectively were each measured in quadruplicate and averaged, showing the mean \pm SD. The X-ray R_g values are shown for PBS-50 (\square and \blacksquare), PBS-137 (\circ and \bullet) and PBS-250 (\diamond and \blacklozenge). The corresponding X-ray $I(0)/c$, R_{XS-1} and R_{XS-2} values are likewise shown. The fitted lines show the mean values in PBS-50 (\cdots), PBS-137 ($- -$) and PBS-250 ($—$) buffers. For IgG1 6a, the $I(0)/c$ values were similar at 0.0187, 0.0158 and 0.0173 for PBS-50, PBS-137 and PBS-250 respectively. For IgG1 19a, the $I(0)/c$ values were also similar at 0.0178, 0.0194 and 0.0188 respectively.

B, the neutron values for IgG1 6a correspond to single measurements in PBS-137 (²H₂O). The R_g values at 6°C (∇ and \blacktriangledown), 20°C (\circ and \bullet) and 37°C (\triangle and \blacktriangle). The fitted lines show the mean values at each temperature: 6°C (\cdots), 20°C ($- -$) and 37°C ($—$).

FIGURE 8. X-ray and neutron distance distribution analyses $P(r)$. The positions of the peak maxima $M1$ and $M2$ and the maximum length L are arrowed. A, the X-ray $P(r)$ curves for IgG1 6a in PBS-50, PBS-137 and PBS-250 are shown for 0.5 - 2 mg/ml. An additional curve for 4.0 mg/ml is displayed for PBS-137. B, the neutron $P(r)$ curves for IgG1 6a in PBS-137 at 6°C, 20°C and 37°C are shown for 2 - 4 mg/ml. C The X-ray $P(r)$ curves of IgG1 19a for 0.22-1.35 mg/ml in PBS-50, 0.30-1.89 mg/ml in PBS-137 and 0.26-1.62 mg/ml in PBS-250.

FIGURE 9. Summary of the X-ray and neutron $P(r)$ analyses. A,C, the concentration dependence of the peak maxima $M1$ and $M2$ for IgG1 6a and IgG1 19a respectively are shown for PBS-50 (\diamond), PBS-137 (\circ) and PBS-250 (\square). The fitted lines are the mean values in PBS-50 (\cdots), PBS-137 ($- -$) and PBS-250 ($—$) buffers. B, the neutron $M1$ and $M2$ values for IgG1 6a are shown for 6°C (∇), 20°C (\circ) and 37°C (\triangle) in PBS-137 (²H₂O). The fitted lines are the mean values at each temperature: 6°C (\cdots), 20°C ($- -$) and 37°C ($—$).

FIGURE 10. Constrained modelling analysis for IgG1. The 20,000 goodness-of-fit R -factors are compared with the calculated X-ray and neutron R_g values for the IgG1 6a and IgG1 19a models. The 20,000 asymmetric and symmetric models are shown in yellow. The ten best-fit models with the lowest R -factors are shown in green, with the best-fit model shown in pink. The experimental observed R_g values are shown by vertical solid lines with error ranges of \pm 5% shown by dashed lines. A, hydrated X-ray models are compared with experimental X-ray data for IgG1 6a in PBS-50, PBS-137 and PBS-250 at 20°C. B, unhydrated neutron models are compared with the experimental neutron curve for IgG1 6a in PBS-137 in ²H₂O at 20°C. C, hydrated X-ray models are compared with experimental X-ray data for IgG1 19a in PBS-50, PBS-137 and PBS-250 at 20°C.

FIGURE 11. X-ray and neutron scattering curve fits for the best-fit IgG1 models. *A*, the three X-ray fits correspond to IgG1 6a in PBS-50, PBS-137 and PBS-250 at 20°C. *B*, the neutron fits corresponds to IgG1 6a at 20°C in PBS-137 in $^2\text{H}_2\text{O}$. *C*, the three X-ray fits correspond to IgG1 19a in PBS-50, PBS-137 and PBS-250 at 20°C. The experimental data are indicated by black circles and the modelled best-fit scattering curve is indicated by the red line. The insets correspond to the experimental and best-fit modelled $P(r)$ curves, in which $M1$ and $M2$ are arrowed.

FIGURE 12. Sets of ten best-fit IgG1 models. The ten best-fit models from each analysis in Figs. 9 and 10 are shown superimposed upon their Fc region (red). The two Fab regions are shown in green and blue. *A*, IgG1 6a in PBS-50, PBS-137 and PBS-250 (X-rays). *B*, IgG1 6a in PBS-137 in $^2\text{H}_2\text{O}$ (neutrons). *C*, IgG1 19a in PBS-50, PBS-137 and PBS-250 (X-rays).

FIGURE 13. Distribution of the Fab-Fc distances in the human IgG1 models. The three distances between the centre-of-mass of the two Fab and Fc regions are shown, where $d1$ corresponds to the Fab1-Fab2 separation, $d2$ to Fab1-Fc, and $d3$ to Fab2-Fc. These distances are shown in grey for the first 500 models in each of the four sets of 5,000 models after excluding the models showing steric clashes between the Fab and Fc regions. *A*, the 30 best-fit X-ray models for IgG1 6a are highlighted (Fig. 10A); *B*, the 10 best-fit neutron models for IgG1 6a are highlighted (Fig. 10B); *C*, the 30 best-fit X-ray models for IgG1 19a are highlighted (Fig. 10C). The orange circles represent PBS-50, black circles for PBS-137 and green circles for PBS-250.

FIGURE 14. Superimposition of the ten best-fit IgG1 models with their C1q and Fc γ R ligands. The ten X-ray best-fit IgG1 models in PBS-137 (Fig. 12A,C) are shown superimposed upon their Fc region (red), together with the crystal structure of the C1q globular head (yellow: PDB code 1PK6) or the crystal structure of the Fc (red)-Fc γ RIII (cyan) complex (PDB code 1E4K).

A, C1q head docked with IgG1 6a.

B, C1q head docked with IgG1 19a.

C, Fc γ RIII-Fc superimposed with IgG1 6a.

D, Fc γ RIII-Fc superimposed with IgG1 19a.

FIGURE 15. Comparison of the human IgG1 and IgG4 complexes with their ligands. *A*, best-fit model of IgG1 6a. *B*, best-fit model of IgG1 19a. *C*, best-fit model of IgG4(Ser²²²). C1q is shown in yellow, and Fc γ RIII is shown in cyan.

Table 1. Modelling searches of the X-ray and neutron scattering and sedimentation coefficient data for human IgG1

	Filter	Models	Spheres ^a	R_g (nm) ^b	R_{xs-1} (nm)	R_{xs-2} (nm)	D_{max} (nm)	R-factor (%)	$s_{20,w}^0$ (S) ^c
X-ray data IgG1 6a									
IgG1 X-ray models	None	20,000	1056-1690	2.91-7.47	0.04-3.47	0.11-2.81	n.a.	n.a.	n.a.
IgG1 b12 (PDB ID: 1HZH)	n.a.	n.a.	1618	5.12	2.60	1.56	n.a.	n.a.	6.84; 6.57
X-ray fit, 2 mg/ml, PBS-50	R_g, R_{xs} , spheres	10	1599-1634	5.09-5.26	2.56-2.66	1.29-1.42	n.a.	3.0	6.67-6.77; 6.39-6.58
Experimental data	n.a.	n.a.	n.a.	5.21 ± 0.03 ; 5.25 ± 0.05	2.57 ± 0.04	1.42 ± 0.06	16	n.a.	6.42
X-ray fit, 4 mg/ml, PBS-137	R_g, R_{xs} , spheres	10	1600-1635	5.14-5.26	2.58-2.68	1.37-1.46	n.a.	3.1	6.67-6.76; 6.37-6.54
Experimental data	n.a.	n.a.	n.a.	5.20 ± 0.06 ; 5.23 ± 0.03	2.61 ± 0.02	1.42 ± 0.01	16	n.a.	6.42
X-ray fit, 2 mg/ml, PBS-250	R_g, R_{xs} , spheres	10	1594-1624	5.00-5.18	2.61-2.71	1.38-1.48	n.a.	3.0-3.1	6.70-6.82; 6.47-6.73
Experimental data	n.a.	n.a.	n.a.	5.28 ± 0.08 ; 5.31 ± 0.06	2.57 ± 0.05	1.47 ± 0.04	16	n.a.	6.35
Neutron data IgG1 6a									
IgG1 neutron models	None	20,000	862-1284	2.77-6.27	0.05-3.00	0.22-2.49	n.a.	n.a.	n.a.
IgG1 b12 (PDB ID: 1HZH)	n.a.	n.a.	1229	4.79	2.32	1.41	n.a.	n.a.	6.84; 6.57
Neutron fit, 4 mg/ml, PBS-137, 20°C	R_g, R_{xs} , spheres	10	1213-1242	4.93-4.98	2.48-2.56	1.17-1.24	n.a.	2.6-2.7	7.09-7.41; 6.29-6.47
Experimental data	n.a.	n.a.	n.a.	5.18; 5.16	2.45 ± 0.01	1.21 ± 0.01	16	n.a.	6.47
X-ray data IgG1 19a									
X-ray fit, 1.4 mg/ml, PBS-50	R_g, R_{xs} , spheres	10	1606-1642	5.11-5.18	2.55-2.63	1.51-1.58	n.a.	2.8-2.9	6.69-6.78; 6.37-6.66
Experimental data	n.a.	n.a.	n.a.	5.13 ± 0.03 ; 5.17 ± 0.02	2.61 ± 0.07	1.50 ± 0.04	15	n.a.	n.m.
X-ray fit, 1.9 mg/ml, PBS-137	R_g, R_{xs} , spheres	10	1581-1625	4.92-5.10	2.56-2.65	1.41-1.52	n.a.	3.6-3.7	6.79-6.90; 6.53-6.68

Experimental data	n.a.	n.a.	n.a.	4.96; 5.15	2.53 ± 0.02	1.45 ± 0.01	16	n.a.	6.34
X-ray fit, 1.6 mg/ml, PBS-250	R_g, R_{xs} , spheres	10	1618-1655	5.08-5.25,	2.65-2.73	1.43-1.52	n.a.	3.1-3.2	6.63-6.76; 6.40-6.60
Experimental data	n.a.	n.a.	n.a.	5.29 ± 0.04 ; 5.32 ± 0.04	2.63 ± 0.01	1.49 ± 0.01	16	n.a.	n.m.

^a The optimum number of hydrated (X-ray) and and unhydrated (neutron) spheres predicted from the sequence was 1607 and 1220, respectively.

^b The first experimental value is from the Guinier R_g analysis (Fig. 6), and the second one is from the GNOM $P(r)$ analysis (Fig. 8).

^c The first modelled value corresponds to that from HYDRO, and the second one is that from HYDROPRO

n.a., not applicable

n.m., not measured

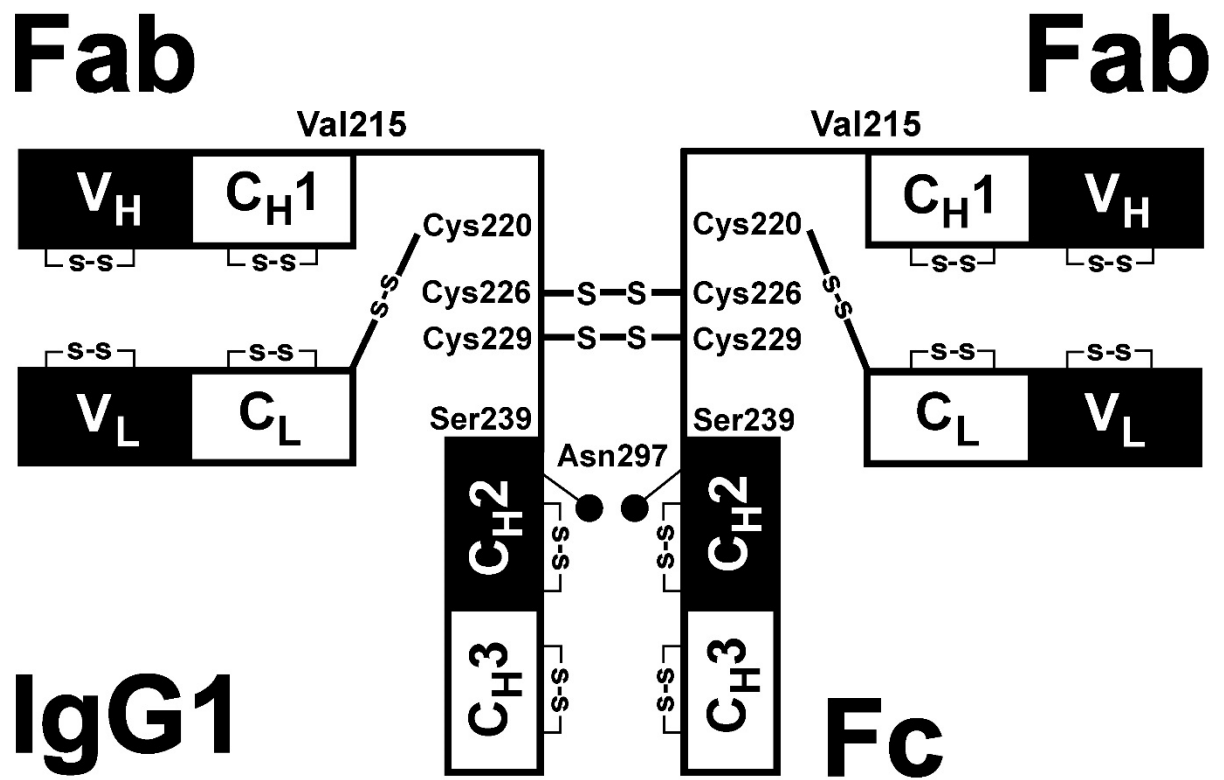


FIGURE 1

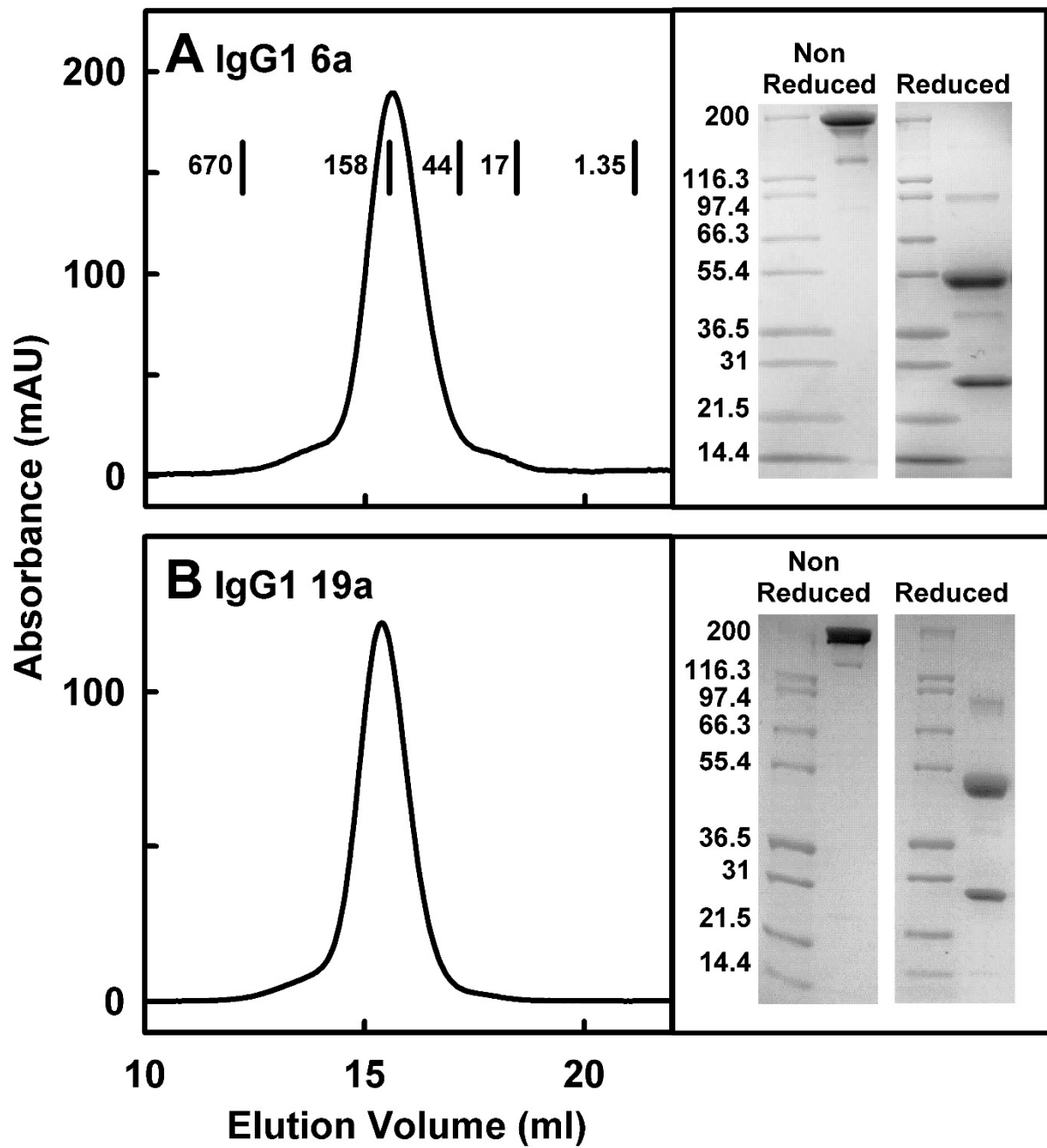


FIGURE 3

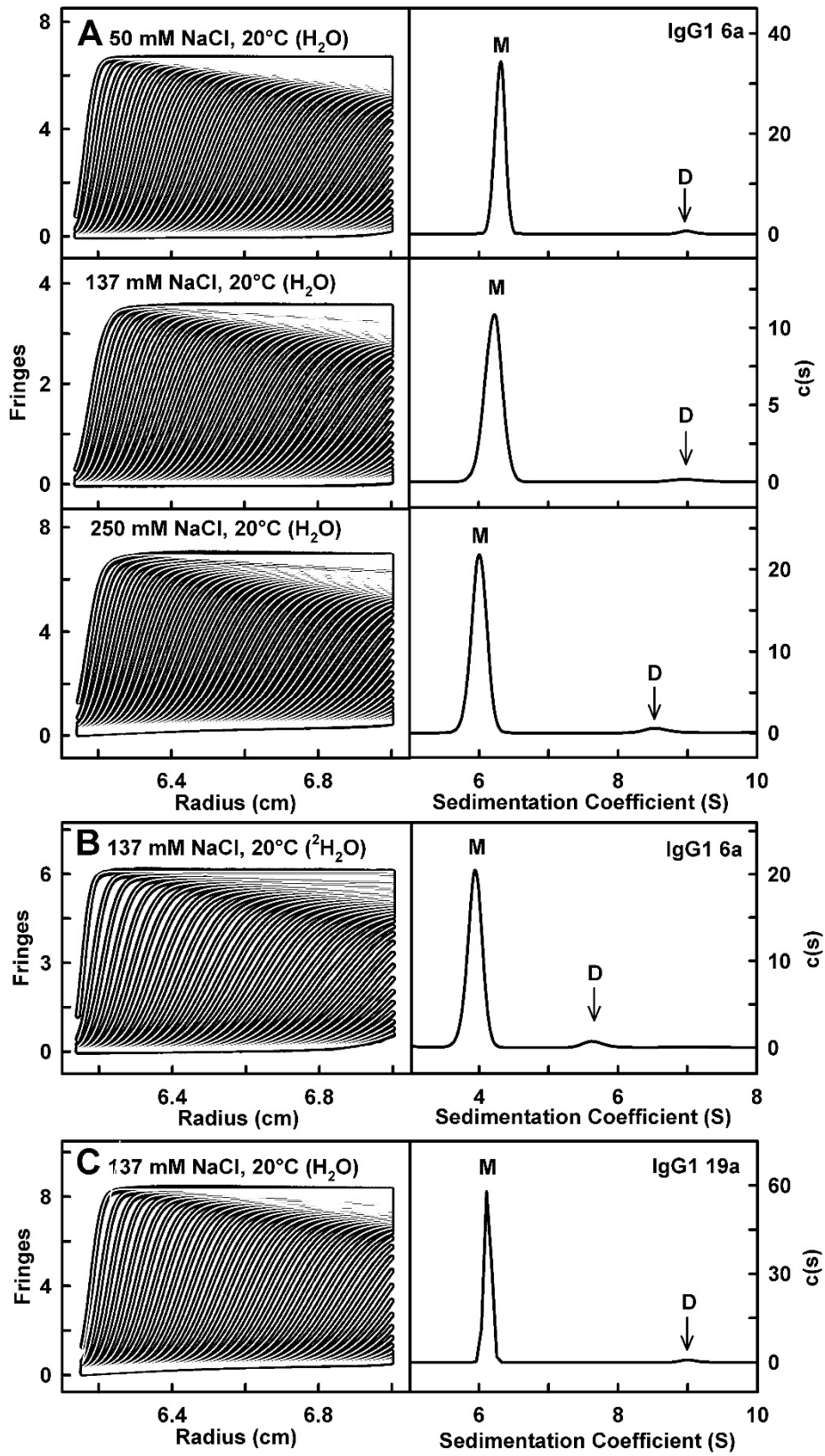


FIGURE 4

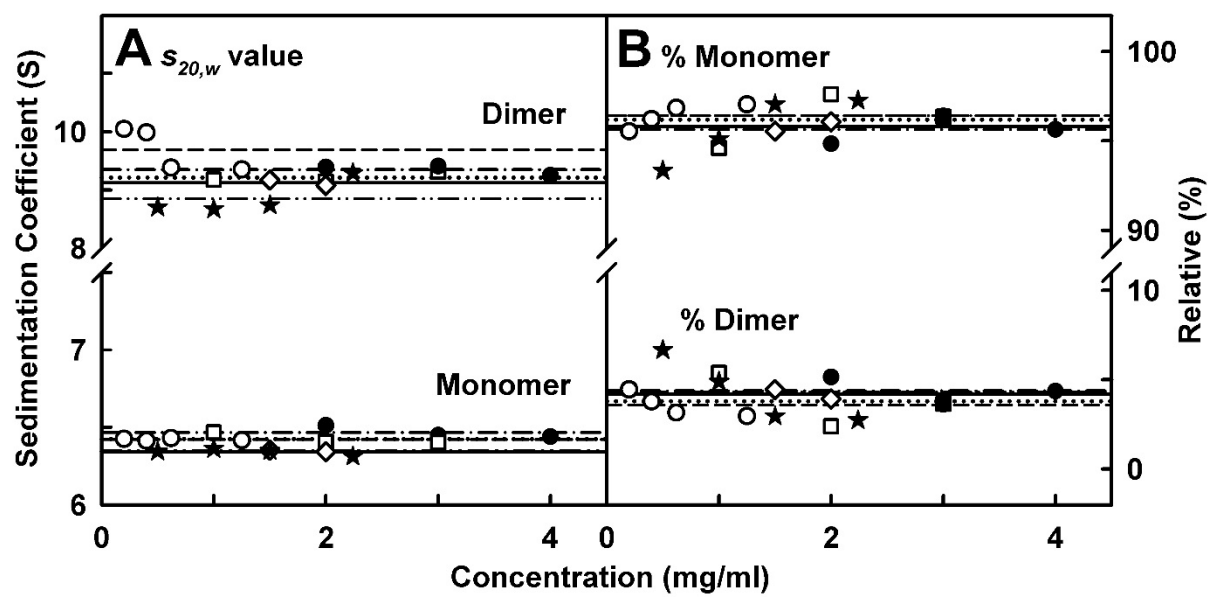


FIGURE 5

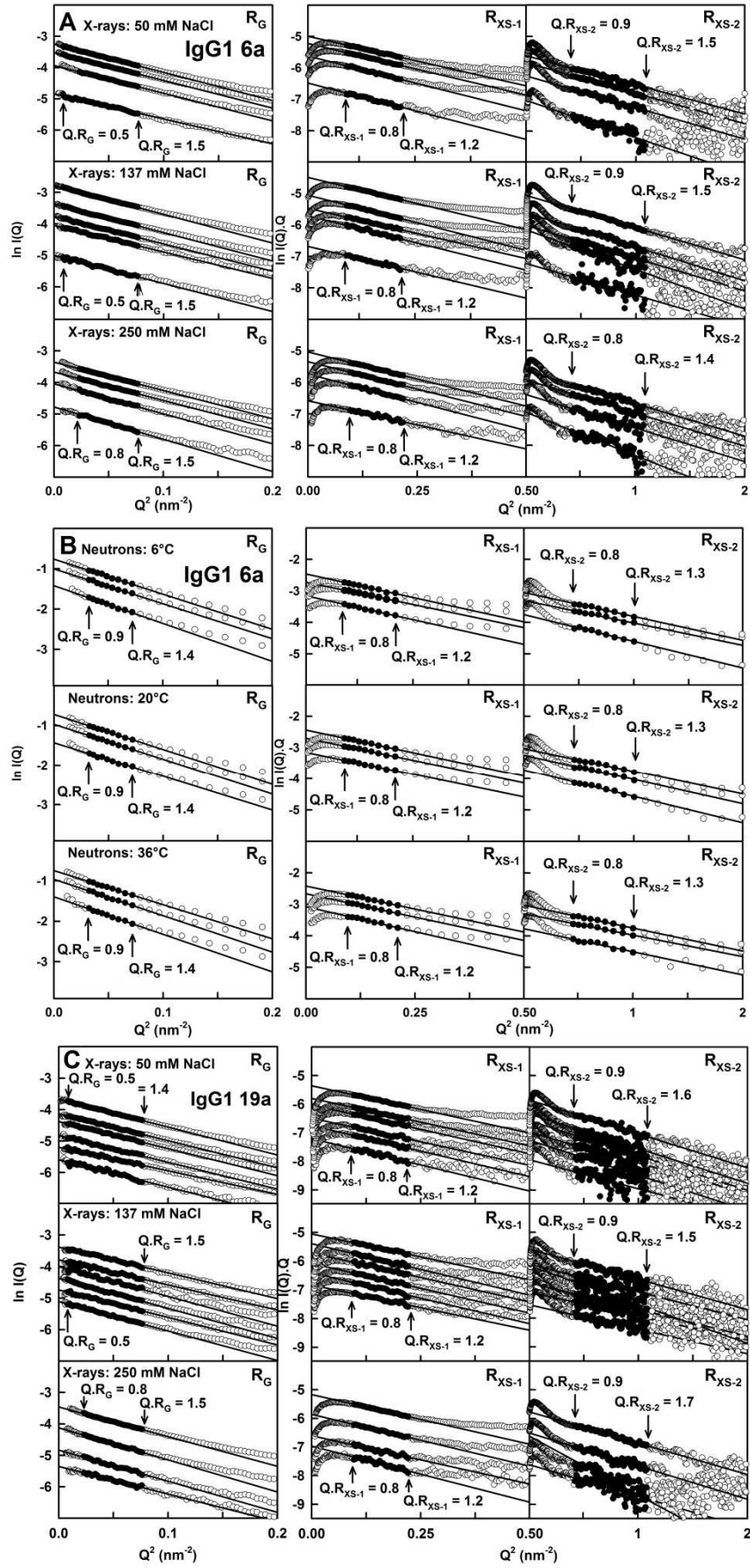


FIGURE 6

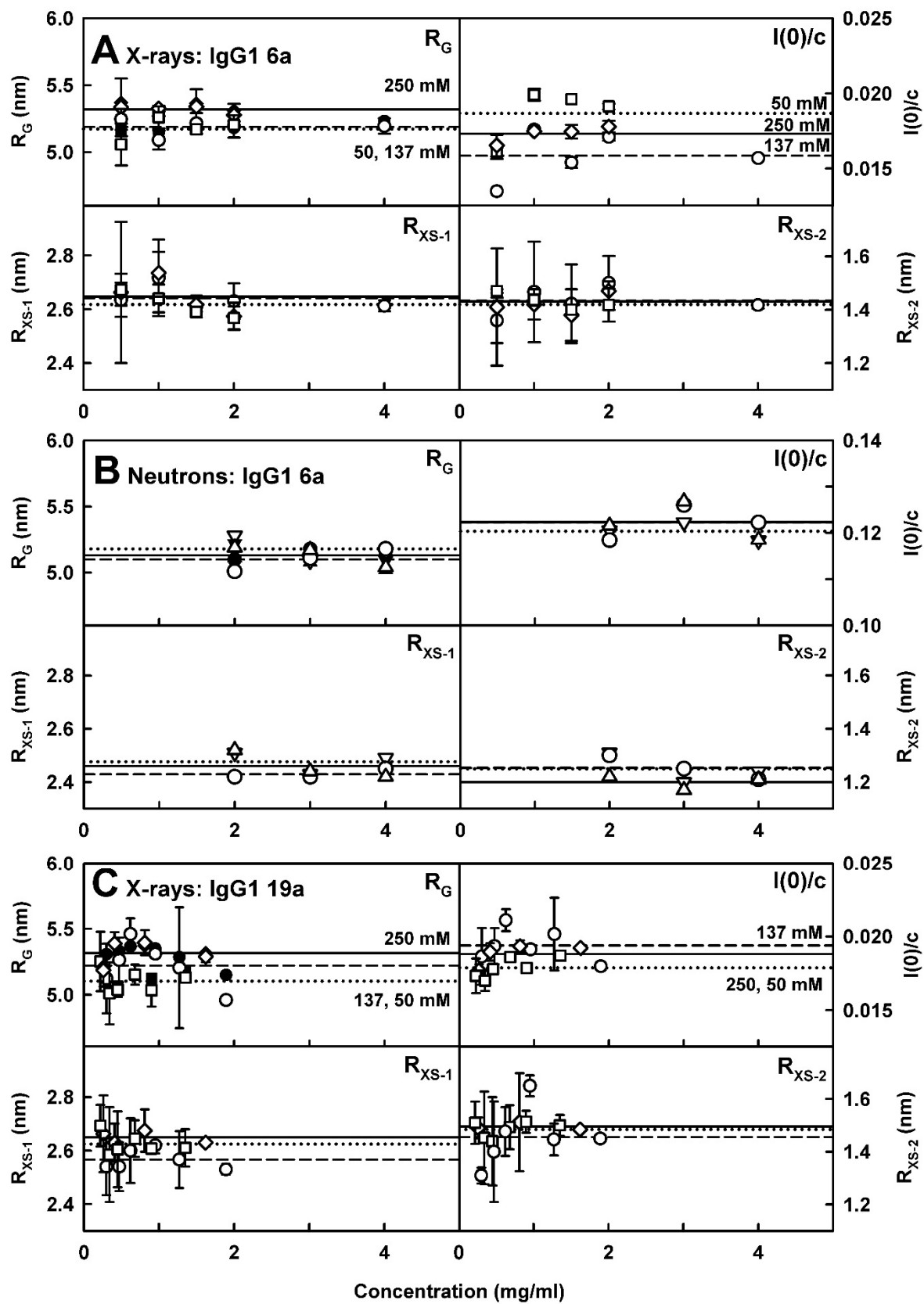


FIGURE 7

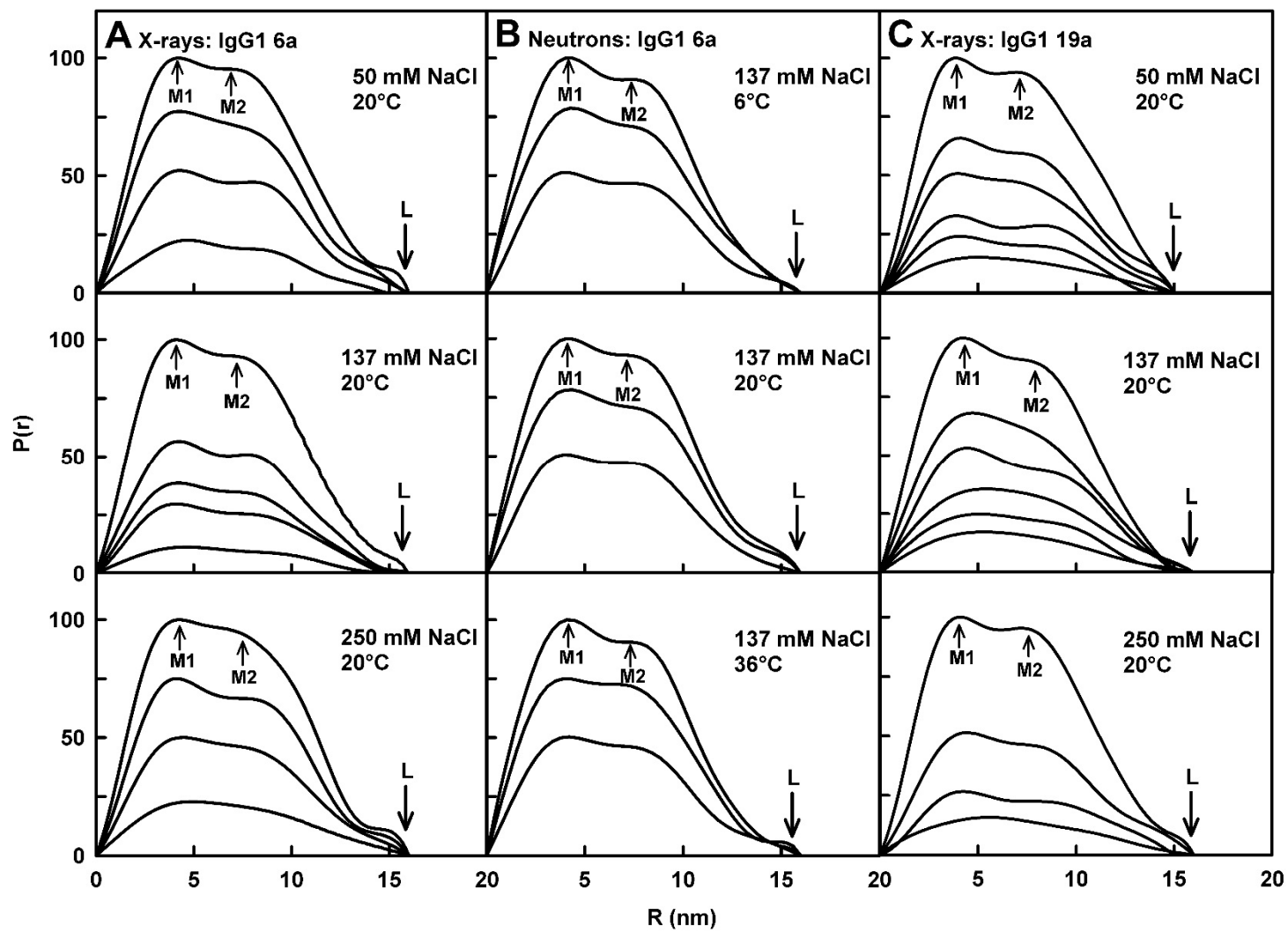


FIGURE 8

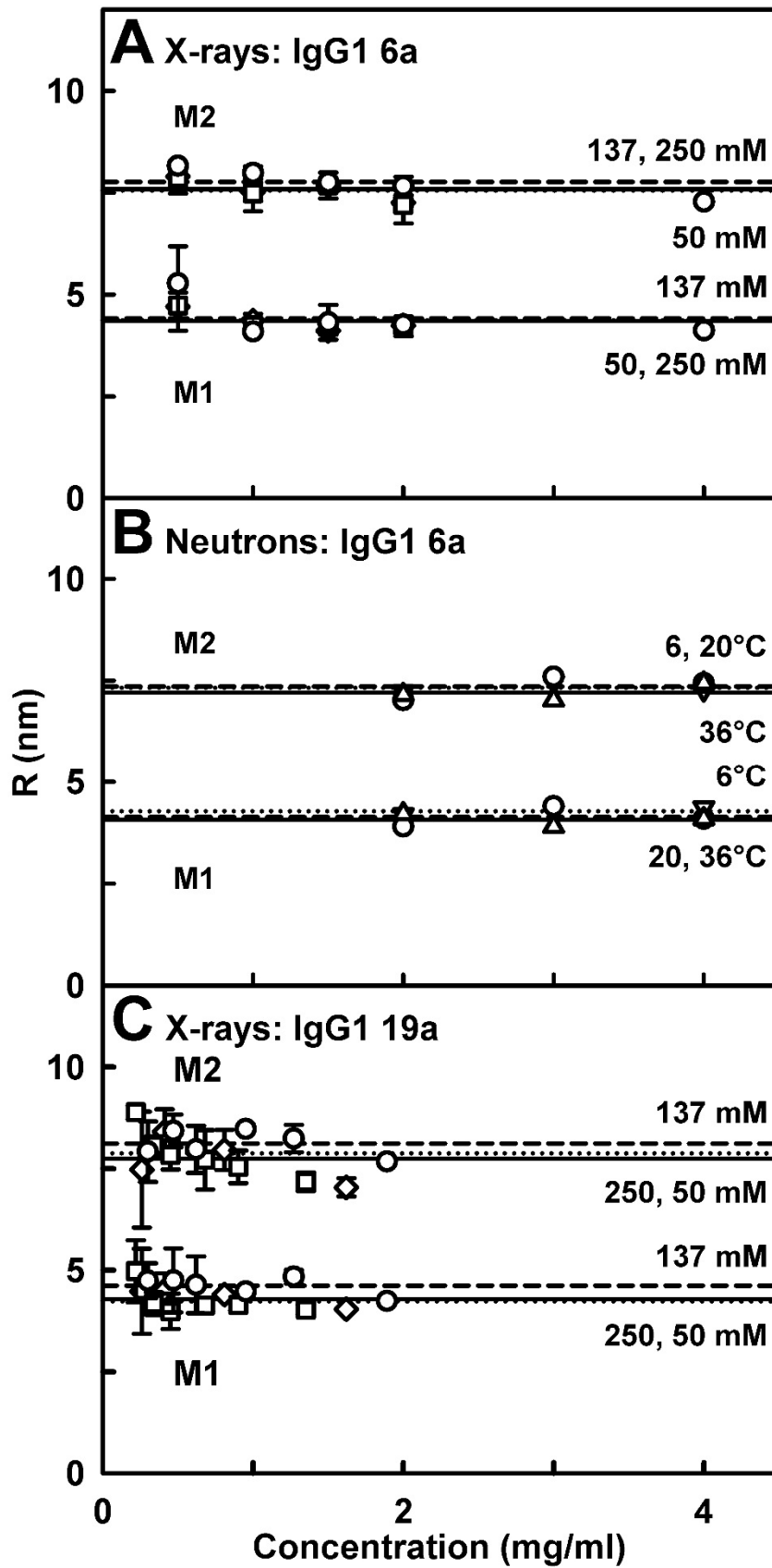


FIGURE 9

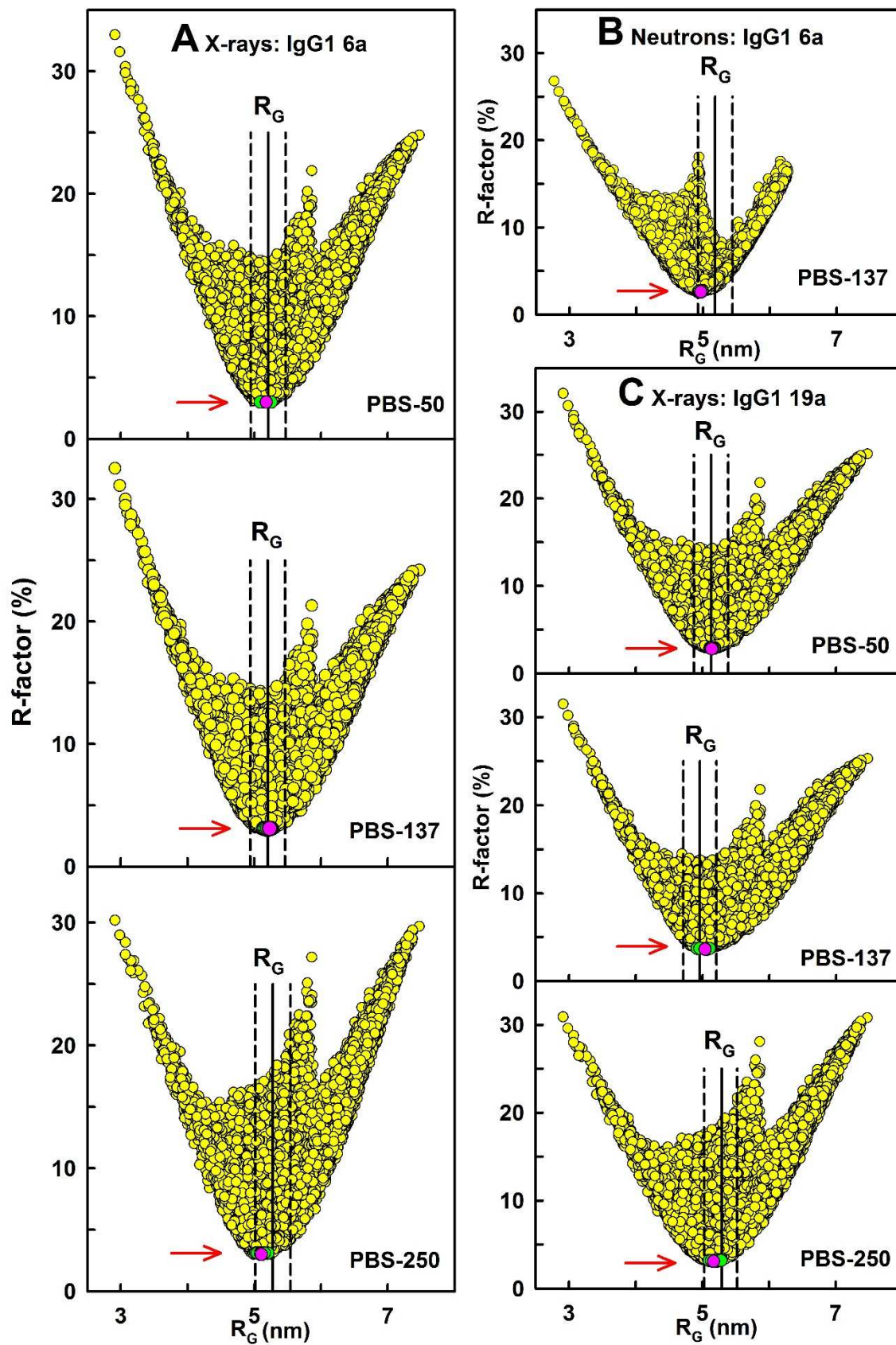


FIGURE 10

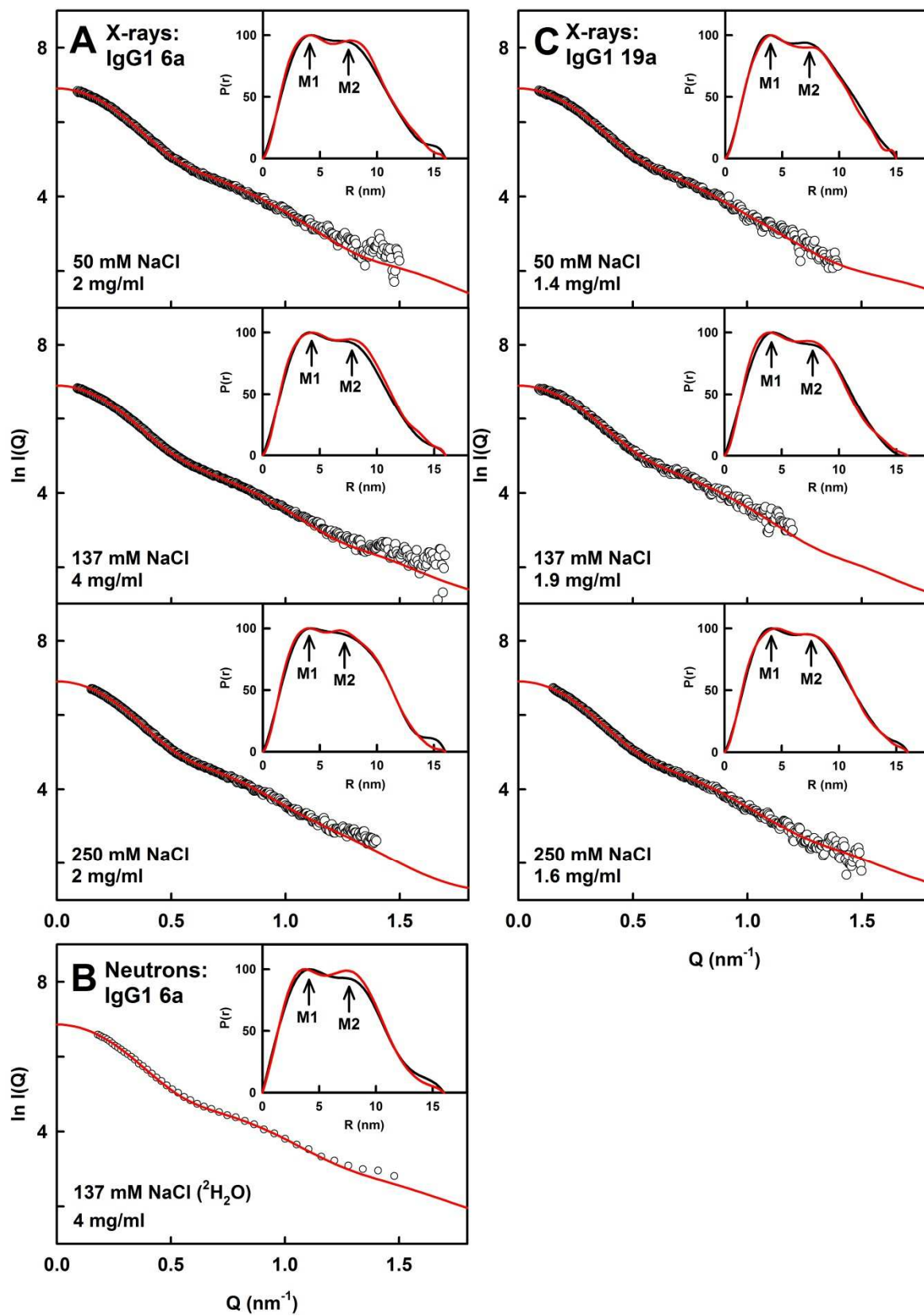


FIGURE 11

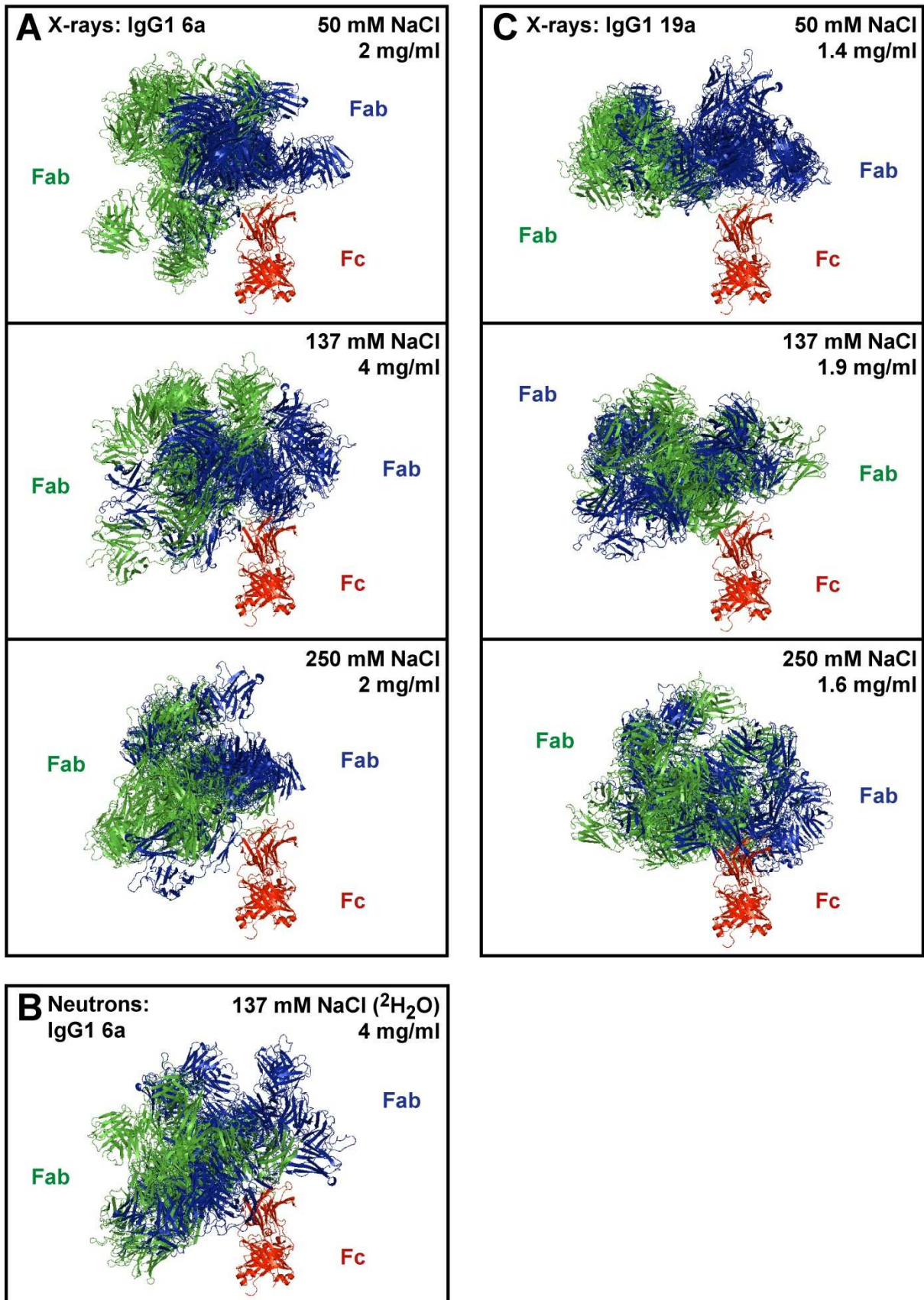


FIGURE 12

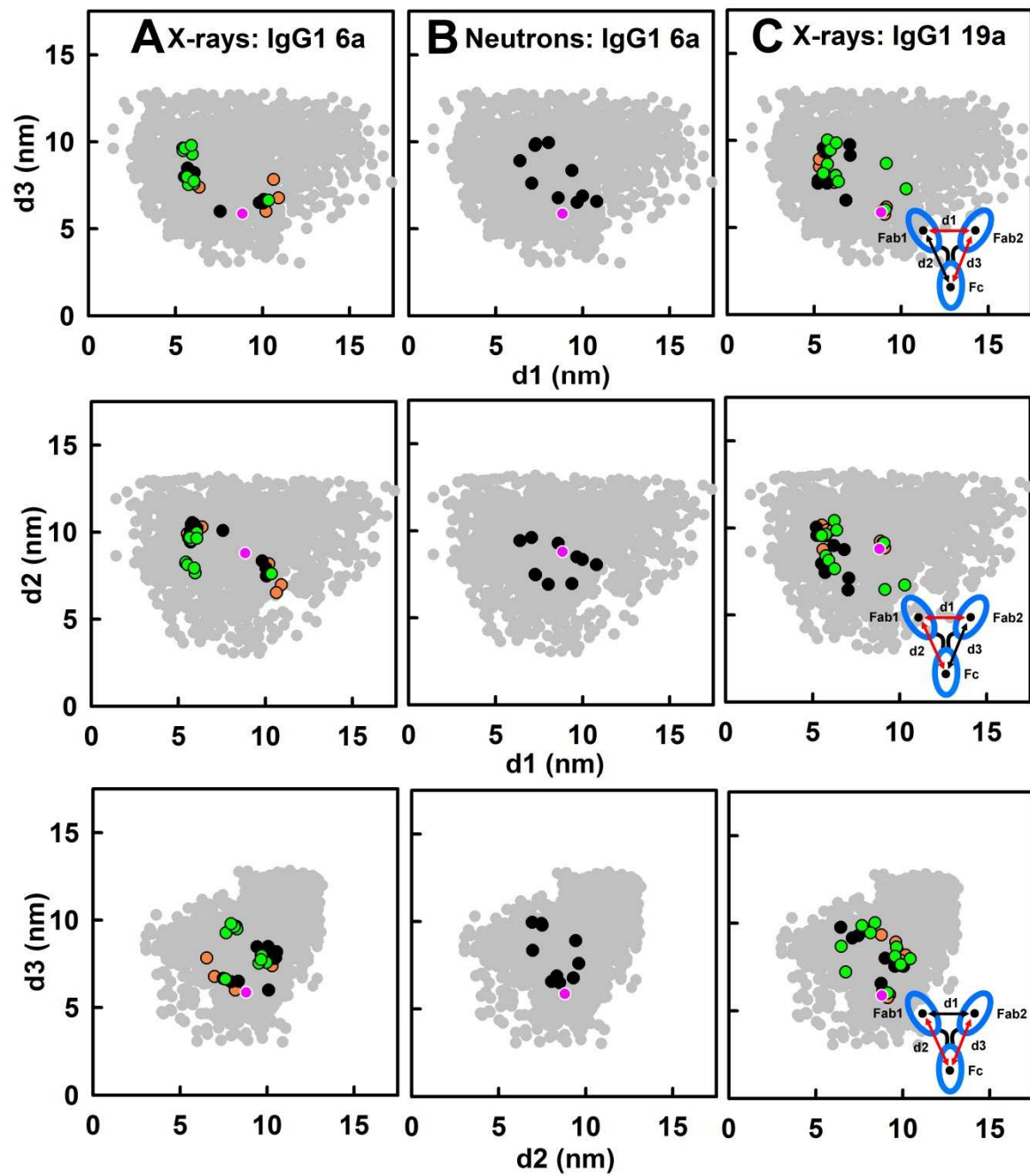


FIGURE 13

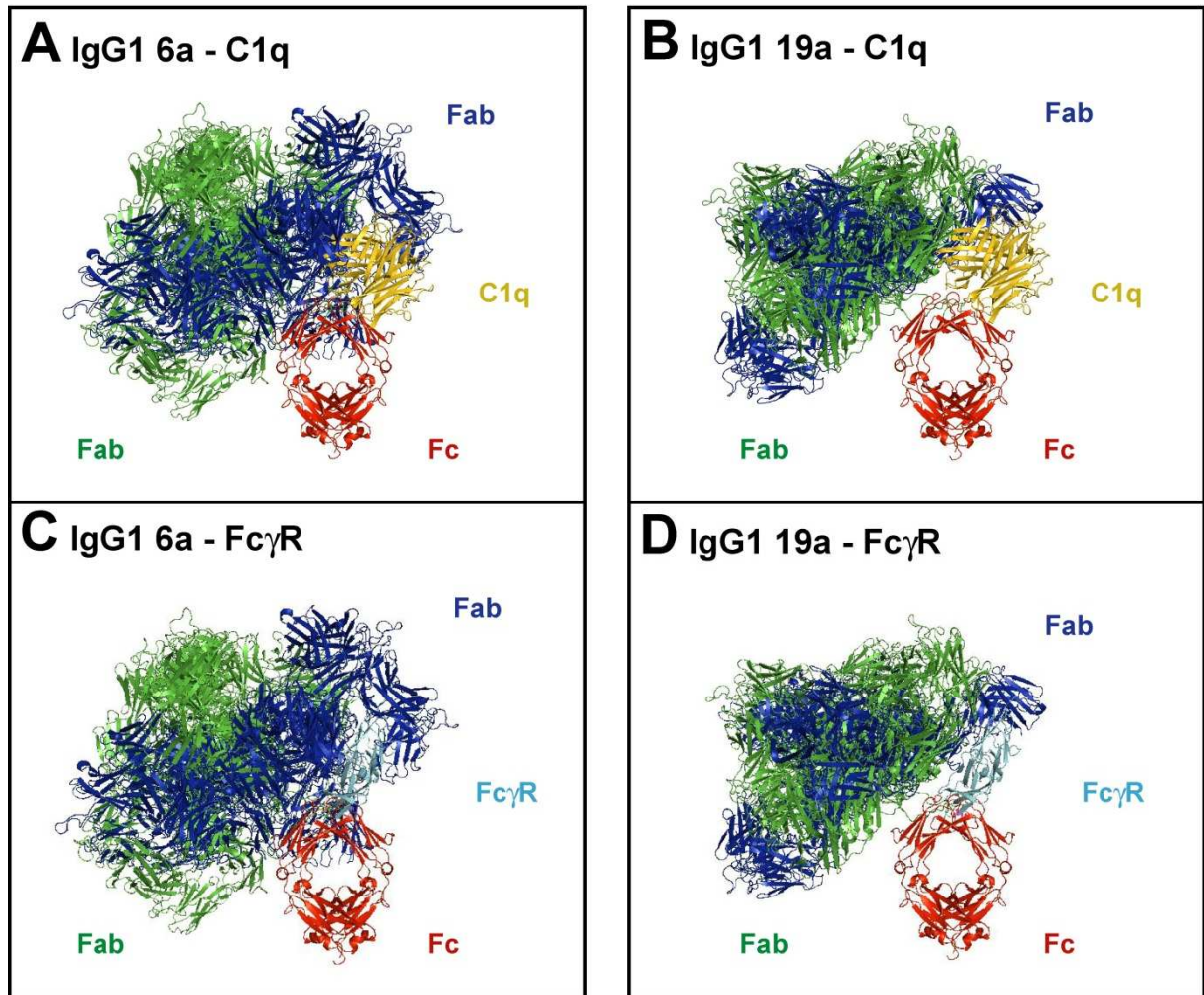
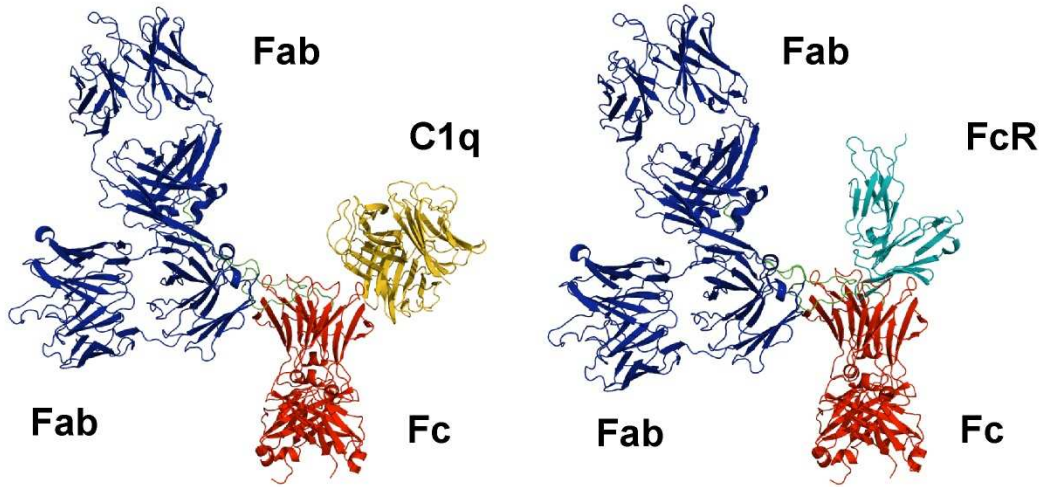
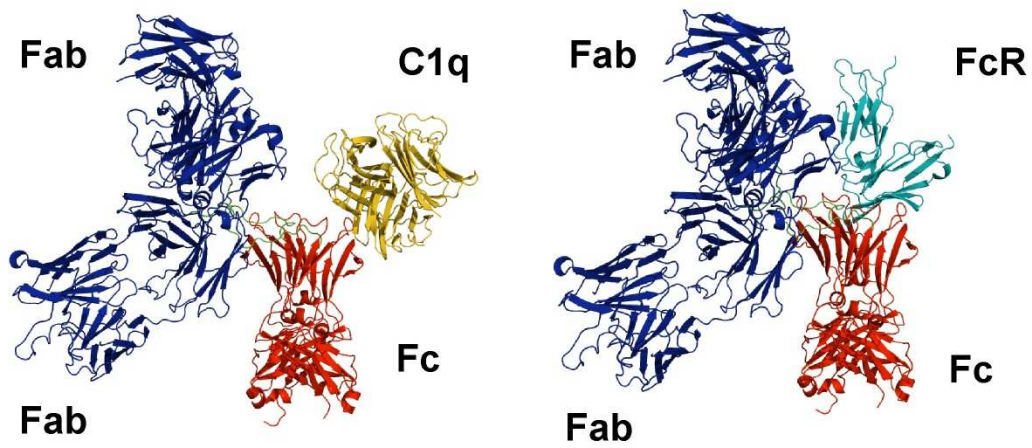


FIGURE 14

A IgG1 6a



B IgG1 19a



C IgG4(Ser222)

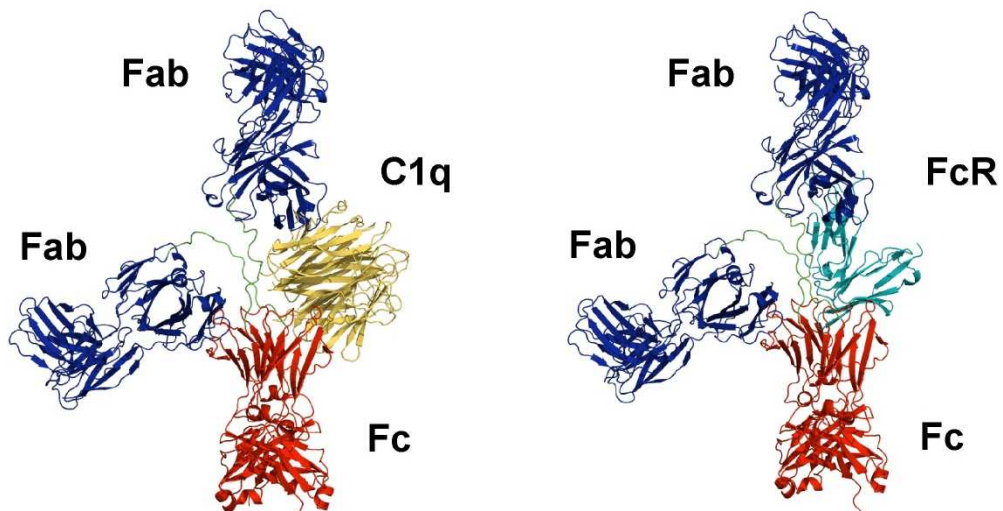


Figure 15